Particuology 119 (2026) 615–635

Contents lists available at ScienceDirect

Particuology

journal homepage: www.elsevier.com/locate/partic

A scalable OpenLB–LAMMPS framework for fully-resolved simulations of hindered settling of arbitrary non-spherical particles

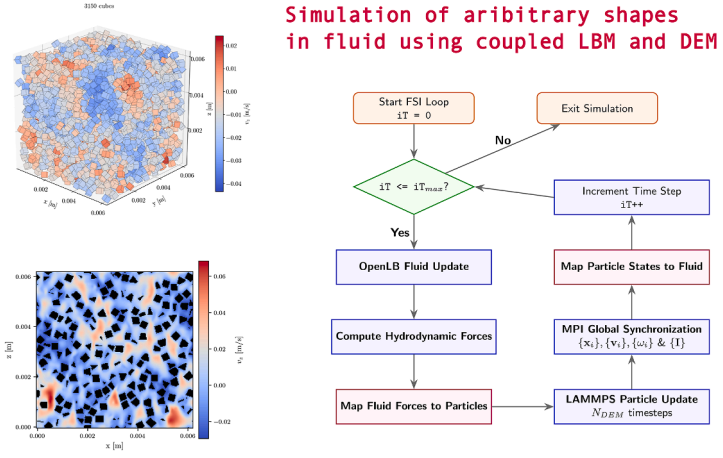
Varghese Babu[a,*], Adrian Kummerländer[b], Mathias J. Krause[b], Santosh Ansumali[c], Dilip Gersappe[a]

[a] Department of Materials Science and Chemical Engineering, State University of New York, 100 Nicolls Road, Stony Brook, 11794-2275, New York, USA
[b] Lattice Boltzmann Research Group, Institute for Applied and Numerical Mathematics, Karlsruhe Institute of Technology, Karlsruhe, Germany
[c] Engineering Mechanics Unit, Jawaharlal Nehru Centre for Advanced Scientific Research, Jakkur, Bengaluru, 560064, Karnataka, India

HIGHLIGHTS

- Couples open-source LAMMPS (DEM) and OpenLB (LBM) for particle-fluid FSI.
- Simulates hindered settling of 100,000 cubes — 10× prior largest study.
- Cubes avoid face-parallel contacts; spheres cluster via contact.
- Velocity correlations scale continuously with system size due to periodic bounds.

GRAPHICAL ABSTRACT



ARTICLE INFO

Keywords:
DEM
LBM
CFD-DEM
Sphere-clump

ABSTRACT

Hindered settling of non spherical particles remains significantly less understood than spherical particles due to the computational challenges in resolving the complex contact mechanics and hydrodynamic interactions. In this paper, we present a scaleable fluid structure interaction (FSI) framework coupling the open-source LBM software in OpenLB (Krause et al., 2021) with the Discrete Element Method (DEM) implemented in LAMMPS (Thompson et al., 2022) to simulate arbitrary shaped rigid bodies in a fluid. Particle contacts are captured using a multi-sphere "clump" representation in DEM, while particle geometries are resolved on the fluid grid via voxelization. We validate our model against single and multi-particle benchmarks, and proceed to study the hindered settling of cubes in systems containing up to $\mathcal{O}(10^5)$ cubes. Our simulations show distinct differences between the settling of cubes and sphere, as cubes form pronounced coordination shells without face-parallel contact, in contrast to the contact-dominated clustering observed in spheres. Our calculations find that periodic boundary conditions might cause the velocity fluctuations along the direction of gravity to remain correlated for even the

*Corresponding author.
E-mail address: varghese.babu@stonybrook.edu (V. Babu).

https://doi.org/10.1016/j.partic.2026.10.024
Received 24 August 2026; Received in revised form 3 October 2026; Accepted 18 October 2026
Available online 27 October 2026
1674-2001/© 2026 Chinese Society of Particuology and Institute of Process Engineering, Chinese Academy of Sciences. Published by Elsevier B.V. This is an open access article under the CC BY license (http://creativecommons.org/licenses/by/4.0/).

largest system size we studied. These findings highlight the role of particle morphology in suspension dynamics and demonstrate a robust framework for simulating large-scale geotechnical and particulate flows.

1. Introduction

Hindered settling is the phenomenon where particle-particle and particle-fluid interactions retard the downward velocity of suspensions with high particle concentrations. Found in many natural and industrial systems, this phenomenon has been subject to extensive experimental and numerical studies. However, numerical models of hindered settling has largely focused on spherical particles. This simplification is inherently limited, as it fails to capture the contact dynamics, interlocking behaviors, and orientational microstructures. In this work, we establish a computational framework to bridge this gap. We have combined a fluid solver, OpenLB, with granular simulation package in LAMMPS, to accurately resolve arbitrary rigid-body shapes and their contact dynamics. This coupled framework for fluid-structure interaction (FSI) is first validated through the study of the hindered settling velocities of sedimenting cubes.

Perhaps the best known result associated with hindered settling is the Richardson-Zaki relation which relates the bulk settling velocity of a suspension of spheres to the packing density (Richardson & Zaki, 1954). This relationship has been validated for spheres through experimental (Chong et al., 1979; Garside & Al-Dibouni, 1977) and numerical evidence (Rettinger & Rüde, 2017b; Willen et al., 2017; Yin & Koch, 2007). Owing to the numerical difficulties in contact detection, there are fewer studies on sedimentation of non-spherical shapes. Some of the recent studies on hindered settling of non-spherical shapes (Fareed et al., 2026; Kundu et al., 2025; Seyed-Ahmadi & Wachs, 2021; Zhang et al., 2016).

Simulations of particles in a fluid typically fall into Euler-Euler or Euler-Lagrange methods. Euler-Euler methods represent the particle phase as continuum. In Euler-Lagrange methods, particles are evolved individually. When particles are simulated individually, the predominant method for simulating particles is DEM (Cundall & Strack, 1979). These simulations are often called CFD-DEM.

There are several commercial and open-source implementation that are available for CFD-DEM. In recent years, Lattice-Boltzmann methods (LBM) have become increasingly prominent and have emerged as a alternative to solving the Navier-Stokes equation directly. LBM has the advantages of being more easily parallelizable and being well-suited for simulating complex geometries. There are different methods developed for particle-fluid interaction in a LBM simulation. They largely fall into momentum-exchange methods (MEM) (Ladd, 1994a, 1994b) and partially saturated methods (PSM) (Noble & Torczynski, 1998). In MEM, a no-slip boundary condition is applied along the surface of the particle. This is in contrast with PSM where each node in the lattice is parametrized by solid fraction and the collision operator in LBM is modified according to the solid fraction. See (Rettinger & Rüde, 2017a; Trunk et al., 2021) for a comparison between the methods. Various implementations of CFD-DEM are listed in Table 1.

Many of the implementations in Table 1 are capable of simulating non-spherical rigid bodies. The main challenge in simulating irregular shaped rigid bodies is contact detection. There are various methods developed for contact detection between general non-spherical shapes. The most common methods are multi-sphere (clump) representation, superquadratics, polyhedral methods and using spherical harmonics. Each method comes with its own advantages and disadvantages, however the "clump" method is the easiest and the most straightforward method to implement. It is also very flexible in that any shape can be decomposed into a collection of spheres. The major drawback of this method is that one might need a large number of spheres for an accurate representation. See (Capozza & Hanley, 2021; Lu et al., 2015; Zhao & Zhao, 2023) for more details.

Despite various available implementations, simulating $\mathcal{O}(10^5)$ arbitrary rigid bodies still remains a major computational challenge. To the best of authors knowledge, openHFDIB-DEM (Studeník et al., 2024) is the only framework that has demonstrated such a capability. To address this gap, in this article we couple LAMMPS (Thompson et al., 2022) and OpenLB (Krause et al., 2021), both designed and capable of large scale parallel simulations. We use the clump multi-sphere representation in LAMMPS for rigid bodies and make use of the FSI (fluid-structure interaction) module of OpenLB to create a fully-resolved LBM-DEM simulation of arbitrary shaped rigid bodies. Presence of the arbitrary solid bodies is represented as a time-dependent lattice porosity field on the Eulerian grid.

Table 1
Summary of commercial and open-source CFD-DEM. Here by "not demonstrated", we mean that we could not find an implementation in the official website/article.

Framework/Software	Fluid solver	DEM engine	License type	Notes
CFDDEM-Coupling (Goniva et al., 2012)	OpenFOAM (Weller et al., 1998)	LIGGGHTS (Kloss et al., 2012)	Open-source	Non-spherical clump representation available only in commercial version.
YADE (Smilauer et al., 2023)	OpenFOAM	YADE	Open-source	Supports polyhedral and clump representation for DEM but fluid coupling of non-spherical particles not demonstrated.
MFiX (Syamlal et al., 1993)	Built-in	Built-in	Open-source	Capable of simulating rigid body shapes in a fluid. Rigid bodies can be represented as "clumps" or using super quadratics.
Lethe-DEM (Blais et al., 2020)	Built-in	Built-in	Open-source	Support for resolved non-spherical particles not demonstrated.
openHFDIB-DEM (Studeník et al., 2024)	OpenFOAM	Built-in	Open-source	Demonstrated $\mathcal{O}(10^4)$ concave non-spherical rigid body + fluid simulations.
Ansys Fluent + Rocky (Fluent, 2023)	Ansys-Fluent	Ansys Rocky	Commercial	-
Commercial CFDDEM-coupling	OpenFOAM	LIGGGHTS	Commercial	-
LBDEMcoupling (Seil & Pirker, 2016)	Palabos (Latt et al., 2021)	LIGGGHTS	Open-source	Non-spherical particle simulations not-demonstrated
LAMMPS-LBM-PSM (Najuch & Sun, 2019)	LBM	LAMMPS	Open-source	LBM is integrated into LAMMPS, non-spherical particles not-demonstrated
LIGGGHTS-Palabos (Ahmadian & Zheng, 2024)	Palabos	LIGGGHTS	Open-source	Non-spherical particle is used as a clump for fluid-structure interaction
OpenLB (Krause et al., 2017)	OpenLB	Built-in	Open-source	Support for only convex shapes
LEDDS (Maggio-Aprile et al., 2025)	LBM	Built-in	Open-source	Supports only spheres and ellipsoids
WaLBerla (Bauer et al., 2021)	LBM	MESA-PD (Eibl, 2021)	Open-source	Supports convex polyhedral representation through MESA-PD

We use the LAMMPS-OpenLB framework to study hindered settling of cubes with the aim of understanding the microstructure. We first validate our framework through simulations of spheres and highlight the differences between cubes and spheres during sedimentation.

2. Models and methods

The simulation consists of using the Lattice-Boltzmann Method (LBM) for the fluid and Discrete-Element-Method (DEM) for the rigid bodies. An important feature of these simulations is the "clump" representation of rigid bodies. We use the "CLUMP" package to generate the overlapping sphere representation of any arbitrary shape (Angelidakis et al., 2021). The rigid bodies are represented as a porosity field in LBM using the FSI module and therefore, we can use the irregular shaped rigid body (available to us as an.stl file, for example) directly in LBM. This means that the effect of any particular clump representation of rigid bodies is only indirectly felt by fluid. This crucially differentiates our work from similar work in (Ahmadian & Zheng, 2024) where the rigid body is represented as a collection of spheres in the fluid as well. Representation of the rigid body as sphere clump in the fluid introduces an additional approximation as the fluid-structure interactions are influenced by the clump representation.

2.1. OpenLB-LAMMPS coupling

The simulation consists of running LBM and DEM simulations sequentially. Depending on the details of the particle contact, viscosity of the fluid and the chosen relaxation constant τ, we have two values of timesteps in the simulation Δt_{DEM} and Δt_{LBM}. For most of the cases we have considered here, $\Delta t_{\mathrm{DEM}} < \Delta t_{\mathrm{LBM}}$. Therefore, we simulate $n_{\mathrm{DEM}} = \frac{\Delta t_{\mathrm{LBM}}}{\Delta t_{\mathrm{DEM}}}$ DEM timesteps for every LBM timestep. During these n_{DEM} timesteps, the forces on the DEM particle due to the fluid is kept constant. Forces on the fluid are calculated based on the final positions and velocities of the particles. In the other case where $\Delta t_{\mathrm{DEM}} > \Delta t_{\mathrm{LBM}}$, we simply set $\Delta t_{\mathrm{DEM}} = \Delta t_{\mathrm{LBM}}$.

The full simulation involves exchange of information between the fluid and the rigid bodies. The fluid solver calculates hydrodynamic forces/torques acting on the rigid bodies and these are included in DEM simulation as external forces/torques. After the DEM simulations are completed, the new positions, velocities, orientations and angular velocities are communicated back to the fluid simulation. This is described in the flowchart Fig. 1.

We use OpenLB (Krause et al., 2021) for LBM and GRANULAR package in LAMMPS (Thompson et al., 2022) for DEM simulations. LAMMPS is used as a library with minimal modifications to its source code. Note that although the rigid body is represented in LAMMPS as a collection of overlapping spheres, this representation is only used by LAMMPS for contact detection and force calculation. The dynamics of the rigid body due to contact forces (and the external forces from LBM) is determined by the mass and moments of inertia specified independently through the infile feature of rigid body simulation in LAMMPS. In all the simulations reported here, we use the BGK collision operator for the fluid phase and Hertzian interactions with tangential friction for the particle contacts.

For the fluid side of the FSI, we use a homogenized lattice Boltzmann method (HLBM) based on the Brinkman-Navier-Stokes equations (BNSE) (Krause et al., 2017; Trunk et al., 2021). The bodies are represented on a fixed Eulerian lattice by a time-dependent porosity field $d(\boldsymbol{x}, t)$, and the no-slip condition is imposed through a volume penalization term (Brinkman drag) added to the incompressible Navier-Stokes equations. For a fluid with kinematic viscosity ν, density ρ, and pressure p, this monolithic formulation is governed by:

$$\frac{\partial \boldsymbol{u}}{\partial t} + \boldsymbol{u}\cdot\nabla\boldsymbol{u} = -\frac{\nabla p}{\rho} + \nu\nabla^2\boldsymbol{u} - \frac{\nu}{K(\boldsymbol{x},t)}(\boldsymbol{u}-\boldsymbol{u}_{\mathrm{s}}) \tag{1}$$

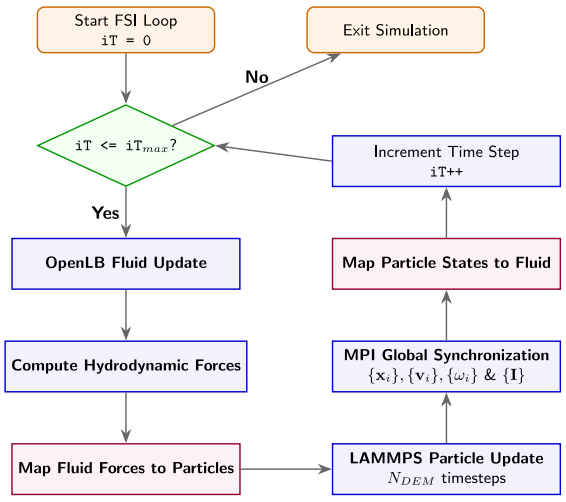


Fig. 1. Flow chart describing our implementation of OpenLB-LAMMPS coupling. $\{\mathbf{x}_i\}$, $\{\mathbf{v}_i\}$, $\{\omega_i\}$ and $\{\mathbf{I}_i\}$ are positions, velocities, angular momentums and the rotated inertia matrix respectively.

where $\boldsymbol{u}$ is the fluid velocity and $\boldsymbol{u}_{\mathrm{s}}$ is the local solid velocity. The permeability $K(\boldsymbol{x}, t)$ is a function of the porosity field, such that the penalization term vanishes in the fluid, where $K \to \infty$, and drives $\boldsymbol{u}$ towards $\boldsymbol{u}_{\mathrm{s}}$ inside the bodies, where K takes its lowest numerically stable value. The motion of the bodies, changes of their geometrical arrangement and their contacts enter the fluid solver only through $d(\boldsymbol{x}, t)$, so that arbitrarily shaped bodies require no special treatment. The penalization is realized as a Kupershtokh forcing term in the collision step, while the hydrodynamic forces and torques acting on the bodies are obtained from a momentum exchange over the lattice links crossing the fluid-solid interface. This Brinkman penalization approach has recently been successfully applied to complex FSI problems, such as wall-modeled large eddy simulations of wind turbine rotors (Kummerländer, Ito, et al., 2026) and vocal fold oscillations (Kummerländer, Tur, et al., 2026).

During the coupled simulation, the structural geometry is resolved via an exact surface voxelization in the fluid solver, while LAMMPS concurrently tracks the contact mechanics and trajectories using the multi-sphere clump representation. This separation allows us to handle complex, arbitrarily shaped geometries contacts. This distinguishes our approach from prior HLBM implementations in OpenLB, such as the work by Trunk et al. (Trunk et al., 2021), which lacked a collision model, and Marquardt et al. (Marquardt et al., 2024a), which was limited to convex bodies. We call our simulations fully resolved in the following sense. The fluid solver represents each body by its actual surface geometry and not by a clump of spheres. This geometry is resolved up to the lattice spacing Δx. The flow around and between the particles is computed directly and no drag closure is used. The hydrodynamic forces and torques follow from the momentum exchange at the resolved interface. The clump is used only by LAMMPS to detect and compute contacts and does not enter the fluid solver. This distinguishes the approach from unresolved CFD-DEM, which models the particles below the grid scale by drag closures. It also distinguishes it from methods that represent the particle shape in the fluid by spheres or that are limited to convex bodies. Flow features smaller than Δx are not resolved. This concerns in particular the lubrication flow in gaps narrower than Δx between approaching surfaces. Fig. 2 illustrates this separation for the Stanford bunny (Turk & Levoy, 1994).The scheme is implemented in the open source LBM framework OpenLB (Krause et al., 2021) as platform-transparent operators, so that the same model definition is executed on CPUs and GPUs. LBM and DEM simulations are detailed in Appendix A.

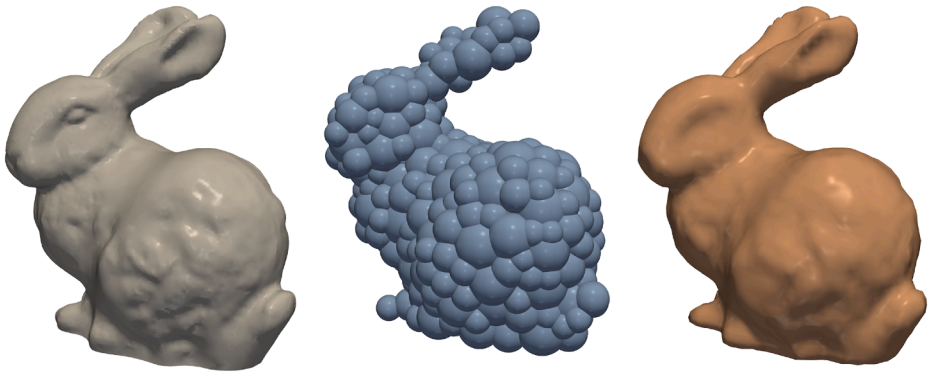


Fig. 2. Representations of the Stanford bunny (Turk & Levoy, 1994). Left: surface mesh of the body. Middle: clump of 400 spheres used by LAMMPS for the contacts. Right: level set $d = 1/2$ of the porosity field seen by the fluid solver at $\Delta x = 7.4$ mm, taken from the simulation in Section 4.3. The fluid solver resolves the actual shape up to the lattice spacing, while the clump only enters the contact model.

3. Validation

We test our implementation by validating sphere settling simulation in a fluid. Our initial set of simulations model three cases: the settling of a single sphere in a fluid, sphere-wall collision, and the calculation of the drag force on a periodic array of spheres.

3.1. Terminal velocity of a single sphere

We reproduce here the validation of the simplest case of a sphere settling in a fluid as discussed in Ten Cate et al. (2002). The experimental setup involves dropping a sphere in a viscous fluid. We compare "Case E1" and "Case E2" in Ten Cate et al. (2002) corresponding to a Reynolds number of ≈ 1.5 and ≈ 32.2 respectively. Our results as shown in Fig. 3a show a good agreement with experimental results. The parameters used for this simulation is presented in Table 2.

3.2. Sphere-wall collision in a fluid

We compare an experimental result of a metallic sphere bouncing on a surface in a viscous liquid from Li et al. (2012) with our numerical method in Fig. 3 b. The presence of lubrication force as the sphere approaches the wall is not captured in our simulations as the gap between the two surfaces become smaller than the lattice separation. To match with the experimental data we enlarge the particle radius by 5% as mentioned in Marquardt et al. (2023). The result, which correspond to Case 1 of Li et al. (2012) is shown in Fig. 3 b. As the sphere comes close to the wall lubrication forces become important - we discuss the lubrication force in Appendix F. Note that we do not retain the increased radius for the remaining calculations.

3.3. Drag force on a periodic array of spheres

Another fundamental result relevant for validation of our numerical method is the drag force on a periodic array of spheres. Analytical result exists for this calculation (Hasimoto, 1959; Ladd, 1988; Sangani & Acrivos, 1982). In this test, we follow the numerical setup outlined in Rettinger & Rüde (2017b). We define a domain of $L \times L \times L$ with periodic boundary conditions and place a sphere at the center whose radius is determined by the packing fraction ϕ we are studying. We apply a constant force density to all the fluid nodes f_{fluid}. We then measure the force acting on the sphere and the average velocity in the domain. At steady state, the measured force on the sphere is equal to the total force applied on all fluid nodes. As discussed in Rettinger & Rüde (2017b), in a real system where one measures the drag force on the sphere, that value will include the buoyancy force as well. However, since we are only applying the force to the fluid nodes, the drag force we measure in the sphere is due to the flow of the fluid alone. We need to add back the buoyancy force to the drag force to get the correct measurements. Therefore, total force is $\boldsymbol{F}_t = \frac{\boldsymbol{F}_d}{1-\phi}$. Our results are shown in Fig. 3c. In Appendix B we discuss the effect of τ and resolution on the results.

3.4. Settling velocity of cuboid

For validation of our code for non-spherical shapes, we compare our numerical technique with experimentally observed settling velocity of cuboidal particles as reported in Kwon et al (2025). The settling velocity of a cube can also be calculated using the empirical relation by Haider and Levenspiel (1989). This relationship is given by

$$u_* = \left[\frac{18}{d_*^2} + \frac{(2.3348 - 1.7439\Phi)}{d_*^{0.5}}\right]^{-1} \tag{2}$$

where

$$u_* = u_p \left[\frac{\rho_f^2}{g\mu(\rho_s - \rho_f)}\right]^{1/3}$$

and

$$d_* = d_{\text{sph}} \left[\frac{g\rho_f(\rho_s - \rho_f)}{\mu^2}\right]^{1/3}$$

with u_p being the particle velocity, d_{sph} the equivalent spherical diameter of the cuboid and Φ the sphericity. The fluid and particle parameters are taken from the experimental study Kwon et al. (2025) and are given in Table 2. We consider the glycerol-water mixture studies for comparison. In the simulation we use pressure boundary conditions in the x and y directions and we use bounce-back boundary condition on z walls. The cube is placed with a face parallel to the $x - y$ plane as in Kwon et al. (2025). As shown in Fig. 4, the numerical method underestimates settling velocity when compared to the experimental result. We also show the empirical relationship alongside, which is lower than both numerical and experimental results. As noted in Kwon et al. (2025), the cubes maintain their initial orientation throughout the descent. The likely reason for underestimation is resolution and dependence of τ as highlighted in Appendix D.

4. Results and discussion

4.1. Hindered settling of cubes and spheres

In this section we present the results from the numerical study of hindered settling of spheres and cubes. For comparison between spheres and cubes, we use cubes that are volume-equivalent to spheres while keeping all other parameters fixed. Settling velocity of a collection of

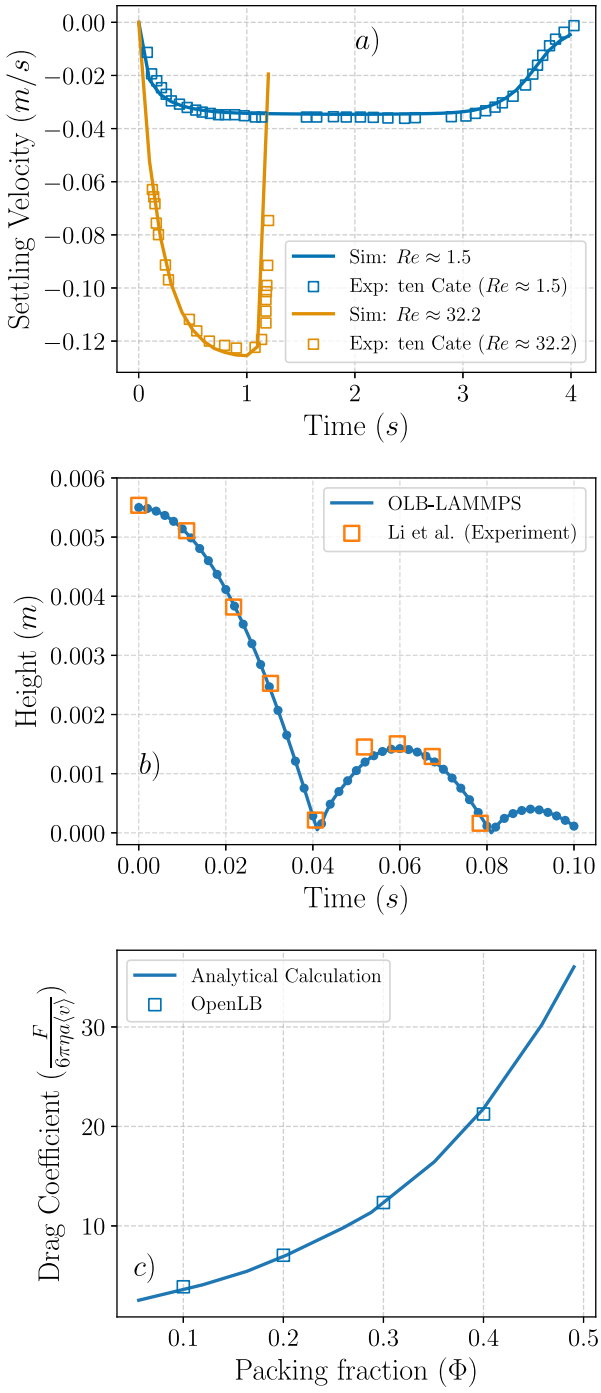


Fig. 3. Sphere simulation in a fluid. (a) Comparison of experimental (Ten Cate et al., 2002) and simulated settling velocities for a sphere falling in a viscous liquid. (b) Comparison of experimental results with numerical results of a sphere-wall collision in viscous liquid. (c) Comparison of the drag coefficient calculated from analytical calculation and from numerical simulations for a periodic array of spheres.

spheres at different packing fractions has been studied numerically Rettinger & Rüde (2017b); Marquardt et al. (2024a); Marquardt & Krause (2024); Trunk et al. (2021); Yin & Koch (2007). Settling dynamics of multiple cubes was studied numerically in Kundu et al. (2025); Marquardt et al. (2024a); Marquardt et al. (2024b); Seyed-Ahmadi & Wachs (2021); Fareed et al. (2026) experimentally in Paul et al. (2017).

Table 2
Summary of physical and numerical parameters used across the four validation cases.

Parameter	Symbol	Value
Terminal velocity of single sphere		
Sphere radius	R	7.5×10^{-3} m
Sphere density	ρ_s	1120 kg/m^3
Fluid density (E1/E2)	ρ_f	970/960 kg/m^3
Fluid viscosity (E1/E2)	μ	0.373/0.058 Pa·s
Reynolds number (E1/E2)	Re	≈ 1.5/≈ 32.2
Relaxation time (E1/E2)	τ	0.661/0.6
Resolution of R	N_{res}	9
Sphere-wall collision in fluid		
Sphere diameter	d_p	9.5×10^{-3} m^1
Sphere density	ρ_{sphere}	7780 kg/m^3
Fluid density	ρ_{fluid}	1203 kg/m^3
Fluid viscosity	μ	50.2×10^{-3} Pa·s
Young's modulus (S/W)	E	20/3.3 GPa
Poisson's ratio (S/W)	ν	0.33/0.24
Domain dimensions	$L_x \times L_y \times L_z$	42×42×50 mm^3
Sphere resolution	$d_p/\Delta x$	32 l.u.
Drag force, periodic array		
Domain size	L	1 m
Grid resolution/dim.	N	64
Viscosity	μ	0.02 Pa·s
LBM relaxation time	τ	0.55
Settling velocity of cube		
Fluid density	ρ_f	1135.19 kg/m^3
Kinematic viscosity	ν	7.325×10^{-6} m^2/s
Particle density	ρ_p	1221.0 kg/m^3
Cube length	a	0.79, 1.00, 1.20, 1.36, 1.59 mm
Domain size	L_x, L_y, L_z	$20a \times 20a \times 50a$
LBM relaxation time	τ	1.0
Resolution	$a/\Delta x$	16

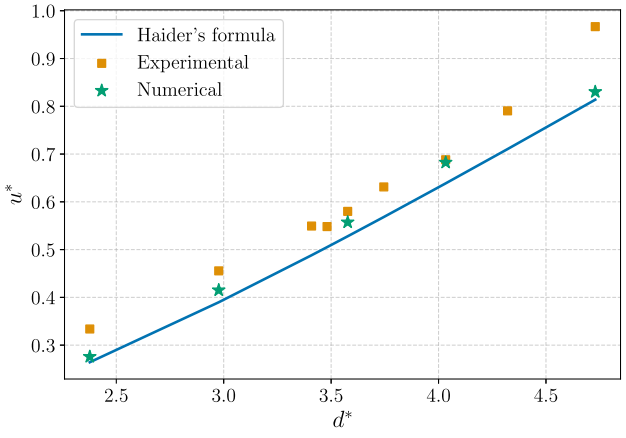


Fig. 4. Settling velocity of cubes. We compare the values calculated from numerical method and empirical formula with experimental results from Kwon et al. (2025).

The simulation is conducted in a domain that is periodic in three directions. To prevent the particles from accelerating infinitely due to gravity, we apply a force to the fluid. This force is periodically adjusted such that the average velocity computed over all nodes is zero. We use the following equation to update the compensating force

$$f_\alpha^{new} = f_\alpha^{old} - K_p \langle v_\alpha \rangle$$

with $K_p = 10^{-2}$ and $\alpha \in [x, y, z]$. This update is performed every 10^{-4} s. The complete set of simulation parameters is specified in Table 3. The Reynolds number is defined as $\text{Re} = \rho_f U_t d_{\text{sphere}}/\mu$ with the sphere diameter d_{sphere}. The cubes are volume equivalent to the spheres. The

velocity $U_t \approx 0.048$ m/s is the terminal velocity of a single sphere (Appendix C). The conversion between lattice and physical units is given in Appendix A.

This numerical method of studying hindered settling using triply-periodic box with a compensating force has been used in various previous studies such as Ladd (1996), Uhlmann and Doychev (2014), Rettinger and Rüde (2017b), Fareed et al. (2026), Fornari et al. (2016), Yin and Koch (2007).

To generate a non-overlapping initial packing, we ran a long simulation (timesteps$> 10^7$ or ~ 220 turnover times) starting from a configuration where spheres are arranged in a square lattice at $\phi = 0.4$. The configuration generated is assumed to have randomized positions and are rescaled down to different packing fractions we study. Given the number of spheres of radius a and the packing fraction ϕ, the domain size can be calculated as $L(\phi, a) = \left(\frac{N\pi a^3}{6\phi}\right)^{1/3}$. The positions of spheres/cubes in a configuration at packing fraction $\phi = 0.4$ is rescaled by $L(\phi_{lower}, a)/L(\phi = 0.4, a)$. The same initial condition is used for both spheres and cubes as the cubes are volume equivalent to the spheres. The hindered settling simulation requires a brief period for the compensating force to stabilize, after which the average velocities of the system remain constant. We notice that the system is characterized by a small drift in the perpendicular direction to gravity which is of an order of magnitude smaller than the bulk terminal velocity. Once the $\langle v_z \rangle$ values have reached their steady state values, we use the last 100 configurations from the trajectory for our analysis. The clump representation of the cube we study and a validation of it is given in Appendix H. The clump representation of the cube used 100 spheres and is shown in Fig. A.10.

4.1.1. Δt_{LBM}, Δt_{DEM} and n_{DEM}

We briefly present the values used for hindered settling simulation of cubes and spheres. Δt_{LBM} can be calculated from the kinematic viscosity ν and space discretization Δx as

$$\Delta t = c_s^2 \left(\tau - \frac{1}{2}\right) \frac{\Delta x^2}{\nu}$$

with τ being the relaxation time. $\Delta x = a/N_{res}$ where a is the radius of the sphere and $N_{res} = 12$ is the resolution.

LAMMPS timestep is given in Table 3 as $\Delta t_{LAMMPS} = 0.05 t_c$ where $t_c = \pi \frac{d_{\text{sphere}}}{2\beta} \sqrt{\frac{\rho_p}{G}}$ known as Rayleigh timestep.

With these information we can calculate $n_{DEM} = \Delta t_{LBM}/\Delta t_{LAMMPS}$.

For $\nu = 10^{-6}$ m^2/s and $a = 0.35$ mm, we have $\Delta x = 2.91667 \times 10^{-5}$ m, then $\Delta t_{LBM} = 1.41782 \times 10^{-5}$ s. Δt_{LAMMPS} works out to 1.0709×10^{-5} s and we round $n_{DEM} = \Delta t_{LBM}/\Delta t_{LAMMPS} = 1$.

Table 3
Summary of physical and numerical parameters used for hindered settling of cubes and spheres. $G = \frac{E}{2(1+\nu)}$ and $\beta = 0.8766 + 0.1630\nu$. LAMMPS contact time t_c is derived from the material properties and particle size: $\pi \frac{d_{\text{sphere}}}{2\beta} \sqrt{\frac{\rho_p}{G}}$ known as Rayleigh Time Step.

Parameter	Symbol	Value
Number of spheres	N	3150 (cubes) 3114 (spheres)
Fluid density	ρ_f	1000 kg/m^3
Fluid viscosity	μ	10^{-3} Pa·s
Particle density	ρ_p	2500 kg/m^3
Sphere diameter	d_{sphere}	0.35×10^{-3} m
Cube dimension	a	0.283×10^{-3} m
Young's modulus	E	5×10^4 Pa
Poisson ratio	ν	0.3
Restitution coefficient	e	0.9
Friction coefficient	μ_t	0.6
Reynolds Number	Re	16.8
Resolution of d_{sphere}	N_{res}	12
Lattice spacing	Δx	2.92×10^{-5} m
LBM time step	Δt_{LBM}	1.42×10^{-5} s
LAMMPS time step	Δt	$0.05 t_c$
LBM relaxation time	τ	0.55
Domain sizes	$L(\phi, a) = \left(\frac{N\pi a^3}{6\phi}\right)^{1/3}$	L (ϕ) 0.0056 m (0.4) 0.0062 m (0.3) 0.0071 m (0.2) 0.0089 m (0.1) 0.0112 m (0.05)

4.1.2. Hindered settling velocity

The u_0 for spheres is -0.0488 m/s and -0.0457 m/s for cubes.

The dependence of the settling velocity of a collection of spheres on the packing density ϕ is empirically given by Richardson-Zaki relation (Richardson & Zaki, 1954). The relation is

$$\frac{\langle u_p \rangle}{u^*} = (1 - \phi)^{\kappa} \tag{3}$$

where

$$\kappa = \begin{cases} 4.65 & \text{Re} < 0.2 \\ 4.35\text{Re}^{-0.03} & 0.2 < \text{Re} < 1 \\ 4.45\text{Re}^{-0.1} & 1 < \text{Re} < 500 \\ 2.39 & 500 \leq \text{Re} \end{cases}$$

Here $\langle u_p \rangle$ is the particle velocity and u^* is the settling velocity of a single particle. First we calculate the terminal velocity of a single cube and a single sphere as ~ 0.0457m/s and ~ 0.048m/s respectively (see Appendix C,D). The terminal velocity for sphere agrees with numerical calculation in Rettinger and Rüde (2017b) for the same system parameters.

The settling velocities of cubes and spheres at different packing fraction is shown in Fig. 5. We also show the Richardson-Zaki relation calculated using Re = 16.8. We also show the result from Batchelor (1972) valid for dilute suspensions. We also show results at similar Re from Climent and Maxey (2003) and Yin and Koch (2007). Numerical results diverge from the empirical formula especially at lower packing fractions. At higher packing fractions, our simulations predict a higher velocity than is found in previous studies of comparable Re. Climent and Maxey (2003) and Yin and Koch (2007) both explicitly add lubrication forces to the study which could be why our results differ from previous at higher packing fractions.

4.1.3. Radial distribution function (RDF)

To understand the structure of cubes and spheres undergoing sedimentation we compute the radial distribution function as given by

$$g(r) = \frac{\langle N_{\text{pairs}}(r, r + dr) \rangle}{\frac{N(N-1)}{2} \times \frac{4\pi r^2 dr}{V}} \tag{4}$$

where the averaging is over configurations at steady state. The denominator term in the above expression is the number of pairs that will be found in a spherical shell of radius r if the particle positions are generated from a uniform distribution. The results for cubes and spheres are shown in Figs. 6 and 7. The RDFs clearly show the difference in structure formed by cubes and spheres. RDF of cubes clearly shows the formation of a first and a second shell. In addition, it is clear that the cubes are not touching each other with their faces parallel - then one would see the first peak before scaled distance 1. For spheres, we observe that, except at the lowest packing fraction we studied, spheres tend to touch each other, with the number of pairs in contact increasing as packing fraction is increased. These figures can be directly compared with results in Seyed-Ahmadi and Wachs (2021), Yin and Koch (2007),

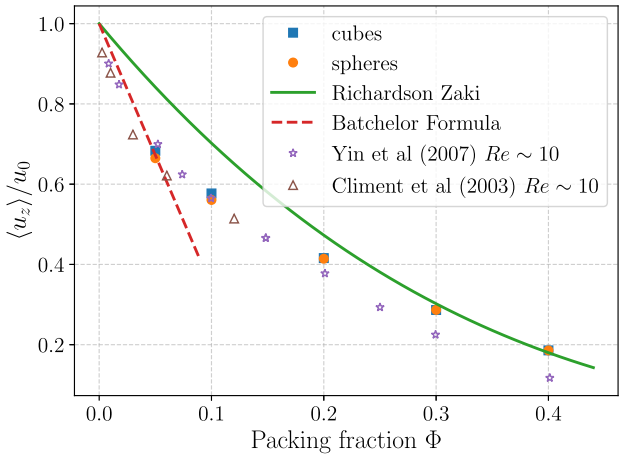


Fig. 5. Hindered settling velocities of cubes and spheres at different packing fractions. We also show comparison with Yin and Koch (2007), Climent and Maxey (2003).

Kundu et al. (2025), Fareed et al. (2026). At low packing fractions $\phi < 0.1$, RDF results of Seyed-Ahmadi and Wachs (2021) and Kundu et al. (2025) shows spheres in contact, which Yin and Koch (2007)'s RDF

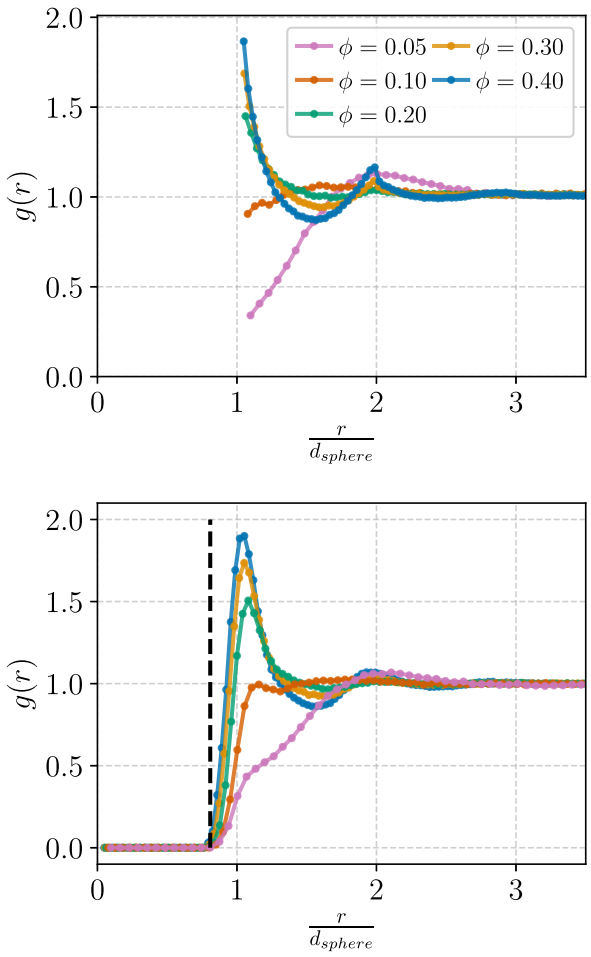


Fig. 6. Radial distributions of spheres (top) and cubes (bottom) for different packing fractions. The black dashed line of the bottom figure indicates the side length of cube $a = 0.000283$m.

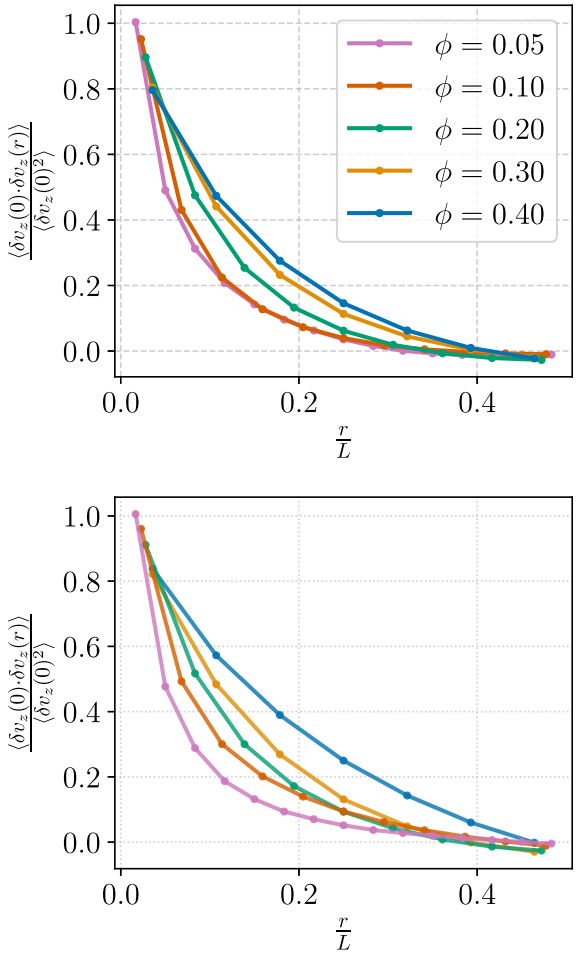


Fig. 7. Correlations in velocity fluctuations of the z component for spheres (top) and cubes (bottom) for different packing fractions.

for Re $\sim$ 10 and our results do not observe. Our RDF of cubes agrees quantitatively with Seyed-Ahmadi and Wachs (2021)'s result for $\phi = 0.2$, while at lower packing fractions, their results predict much larger number near pair contacts. See comparison in Appendix E. It must be noted that simulation in Seyed-Ahmadi and Wachs (2021) are at a higher Reynolds number than here.

Here, we also note the effect of underestimation of lubrication force. As shown in Appendix F, force acting on spheres when the gap between them is smaller than $0.12 \times r_{sphere}$ is underestimated and therefore, RDF values for spheres at close contact maybe not be physical.

4.1.4. 2-Point spatial correlation of velocity

In the steady state, the other natural quantity to calculate is the velocity-velocity correlation in space. Since the system as a whole has a mean velocity in the $-\hat{z}$ direction due to gravity, we measure the correlation between velocity fluctuations. The fluctuation is calculated as $\delta v_z = v_z - v_{\text{mean}}$ where $v_{\text{mean}} = \langle v_z \rangle$. The correlation is calculated by

$$C(r) = \frac{\langle \delta v_z(0) \cdot \delta v_z(r) \rangle}{\langle \delta v_z(0)^2 \rangle}.$$

We show the 2 point correlation of velocity in Fig. 7. Given the periodic boundary conditions, we calculate the correlation function only up-to $0.5L$ where L is the side length of the cubical domain. The main observation here is that correlations in velocity fluctuations stretch across the system for all packing fractions studied. We will come back to

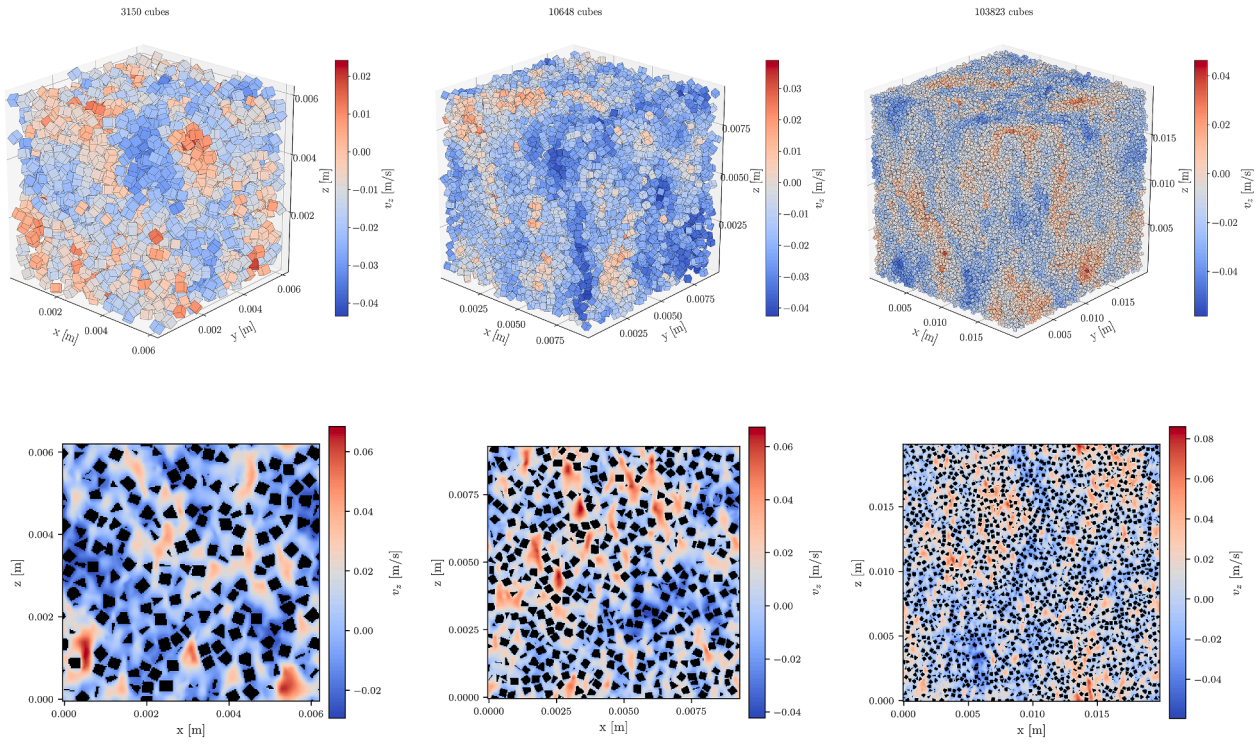


Fig. 8. Visualization of cubes undergoing hindered settling for three system sizes studied at $\phi = 0.3$. The top row shows the cubes colored by v_z for 3150, 10648 and 103823 cubes respectively. The bottom row are slices along the xz plane showing fluid velocities along with the cubes for the corresponding system sizes.

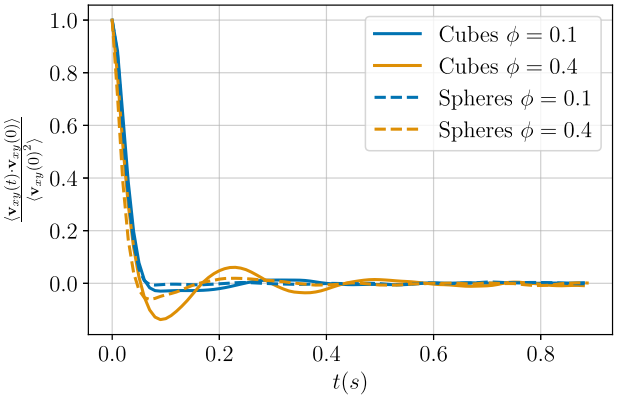


Fig. 9. Velocity-autocorrelation for cubes and spheres at two different packing fractions.

this point in a later section where we analyze systems of different sizes. We also find that correlations are stronger for cubes than for a spheres at a given packing fraction.

4.1.5. Velocity auto-correlation

We calculate velocity autocorrelation for hindered settling of cubes and spheres. We calculate the velocity autocorrelation for x and y direction

$$C(t) = \frac{\langle \mathbf{v}_{xy}(t)\cdot\mathbf{v}_{xy}(0)\rangle}{\langle \mathbf{v}_{xy}(0)^2\rangle}. \tag{5}$$

The results are given in Fig. 9. VACF of cubes at higher packing fraction shows a oscillating decay, similar to an under-damped oscillator. A similar observation is reported in work of Fornari et al. (2016) for the vertical component of velocity, which is a study carried out at much lower packing fractions and higher Re.

4.2. System size dependence

To demonstrate the capability of our framework, we study systems at $22^3 = 10,648$ and $47^3 = 103,823$ cube systems. We study both systems at a $\phi = 0.3$. The correlation functions calculated from these simulations and the settling velocity are shown in Figs. 10 and 11. The primary conclusions from this study is that the average settling velocity and local arrangement of the cubes do not change as we study large systems. However, the 2-pt velocity correlation in space shows that the correlation length scales with the system size even for the largest system size we studied.

Previous works have studied dependence of velocity fluctuations on system size (Guazzelli, 2001; Segre et al., 2001; Segrč et al., 1997) experimentally and Ladd (1988, 1997) numerically. Spatial correlation in velocity fluctuations have been previously reported in Guazzelli (2001), Segrč et al. (1997) experimentally and numerically in Climent and Maxey (2003), Uhlmann and Doychev (2014), Yao et al. (2021). As summarized in Guazzelli and Hinch (2011) and Guazzelli (2001), the velocity fluctuations were found to saturate to a steady value as the box size exceeded $20a\phi^{-1/3}$ in experiments. The initial fluctuations were found to be of the size of the container which would diminish with time and reach a size of $20a\phi^{-1/3}$. Numerically, the packing fraction ϕ and number of particles N and the box dimensions are related as $L^3 = \frac{N\pi a^3}{6\phi}$. For $L^3 > (2 \times 20a)^3\phi^{-1}$, $N \gtrsim 122,000$, which is the minimum size required to observe correlations at the discussed length-scale.

Numerical observations from Climent and Maxey (2003), Uhlmann and Doychev (2014), Yao et al. (2021) show that the correlation in fluctuations along the vertical component of the velocity does not decay to zero even for the largest system, however the system sizes studied are not comparable to the limit observed in the experiments. The largest system size studied here approaches the limit and does not show a system that is uncorrelated spatially.

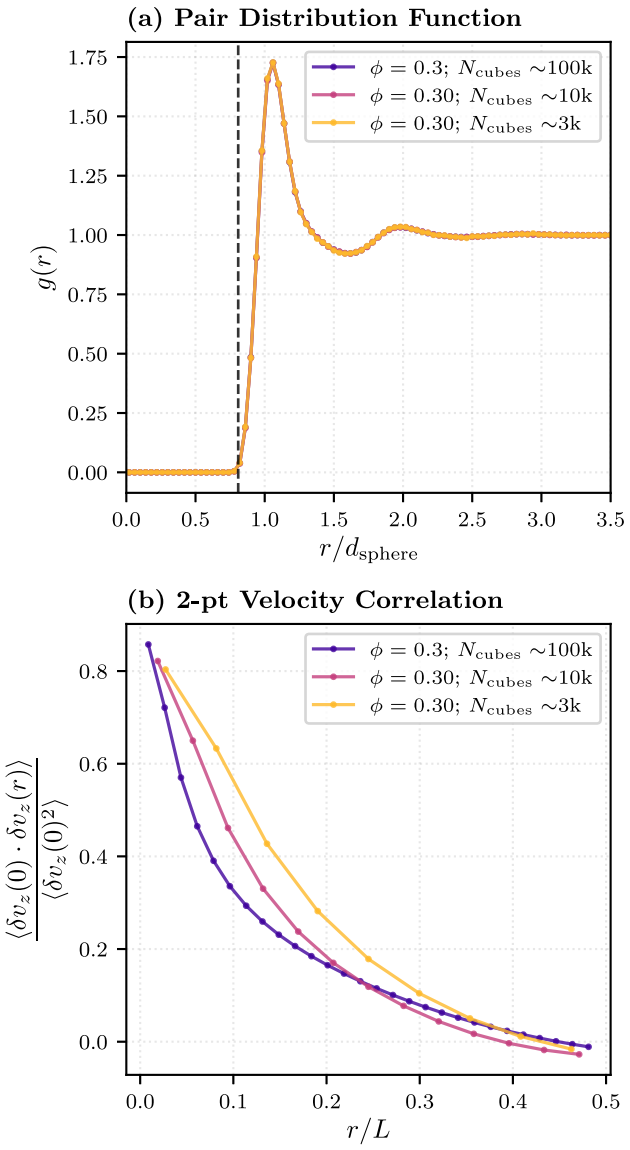


Fig. 10. Correlation functions for different system sizes studied.

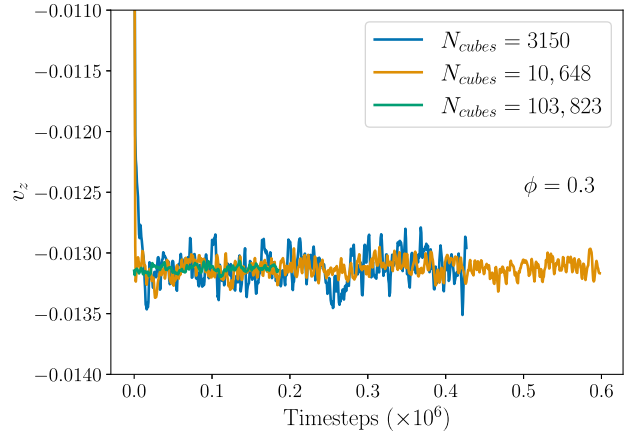


Fig. 11. Terminal velocity v_z at $\phi = 0.3$ for different system sizes. The system size does not strongly affect the terminal velocity of bulk suspensions.

Table 4
Parallel efficiency and scaling across three cube-sedimentation runs at different particle counts. All simulations are ran on AMD EPYC 7643 48-Core Processor.

Particles	3150	10,648	103,823
Lattice nodes (M)	9.53	32.16	314.43
Nodes per particle	3025	3020	3029
MPI ranks	16	64	64
Approx particles per rank	196.9	166.4	1622.2
Avg. MLUPs	24.30	111.58	109.58
MLUPs per rank	1.52	1.74	1.71
Wall-clock time (0.5 s)	3.87 h	2.86 h	28.14 h

As mentioned in Ladd (2002, 1996), this could be an artifact of the periodic boundary conditions applied to top and bottom walls in the system. Details of different systems are given in Table 4. A visualization of the three system sizes studied is shown in Fig. 8 where we can see the system scale correlation in velocities.

4.3. Settling of stanford bunnies

To show that the framework is not restricted to simple or convex shapes, we simulate the settling of 512 copies of the Stanford bunny (Turk & Levoy, 1994). The bunny is a non convex body with thin features such as the ears. Its surface mesh is embedded into the fluid as described in Appendix A, and LAMMPS represents it by a clump of 400 spheres (Fig. 2). Each bunny has a height of about 0.32 m and a density of $\rho_p = 1250\ \text{kg/m}^3$. The bunnies start from rest with random orientations in a regular $8 \times 8 \times 8$ arrangement in a cubic box of side length 4.08 m, which is periodic in all directions. The fluid has the density $\rho_f = 1000\ \text{kg/m}^3$ and the kinematic viscosity $\nu = 10^{-3}\ \text{m}^2/\text{s}$. We use $\Delta x = 7.4$ mm, so that a bunny spans about 43 cells, and $\tau = 0.52$. As in Section 4.1, a uniform force on the fluid balances the net weight of the bunnies. The simulation runs on a single GPU. Fig. 12 shows three snapshots. The regular arrangement breaks up as the bunnies settle, and the bunnies collide, rotate and pass through the periodic boundaries. The mean settling velocity levels off at about 0.7 m/s after about 3 s. A video of the simulation is available at https://www.youtube.com/watch?v=zM0RIz2ZGaE.

5. Conclusions

We have implemented and validated a new framework to simulate irregular shaped particles in a fluid using open-source codes such as OpenLB and LAMMPS. We demonstrate the capabilities of our framework by simulating $\mathcal{O}(10^5)$ cubes in a fluid. This is an order of magnitude larger than Studeník et al. (2024) where they demonstrated $\mathcal{O}(10^4)$ rigid bodies. We have used this capability to study hindered settling of spheres and cubes. Our analysis of local structure of cubes and spheres show qualitative agreement with previously published results in Seyed-Ahmadi and Wachs (2021), Kundu et al. (2025), Fareed et al. (2026), Yin and Koch (2007) although previous studies are at different Re. Spatial correlation in velocity fluctuations calculated at different system sizes indicate that the velocities remain correlated across the system even at the largest system studied. This problem is also addressed in Moriche et al. (2026). This required further analysis and experimentation with different periodic boundary conditions, box dimensions and also perhaps the balancing force acting on the fluid nodes.

The framework can be further optimized in various ways. Currently, the implementation requires LAMMPS and OpenLB to have same number of MPI threads. An optimal number of threads for LAMMPS and OpenLB might be different at different densities which could make the code faster. GPU implementation of DEM simulations is also another direction for optimization. Future versions will include the lubrication force between particles.

Future work will also be able to directly utilize the HLBM moving wall model Kummerländer, Ito, et al. (2026) for turbulent flows of moving arbitrarily shaped particles.

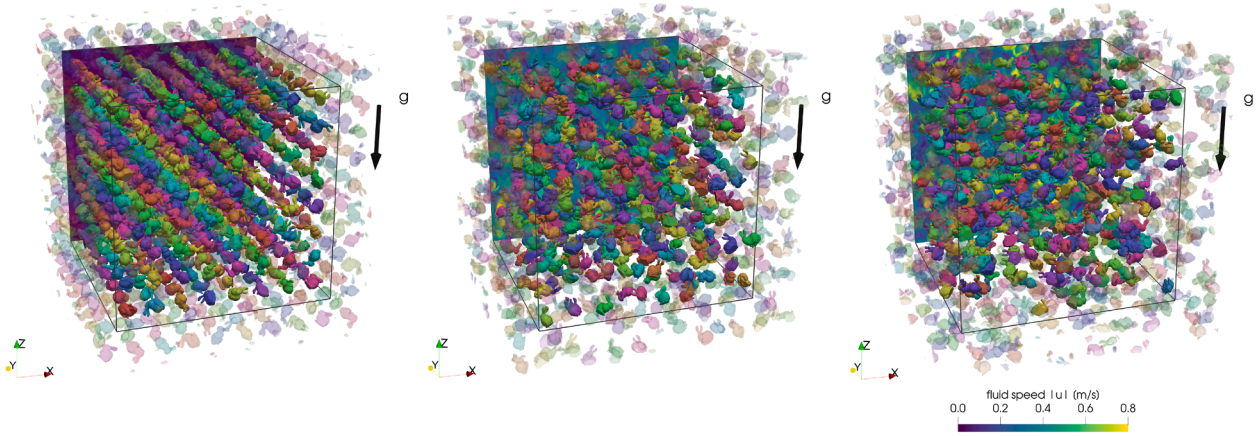


Fig. 12. Settling of 512 Stanford bunnies in a triply periodic box. Snapshots at $t = 0$, 2.5 s and 5 s (left to right). Each bunny keeps its color in all snapshots. The faded bodies outside the box are periodic images. The back wall of the box shows the fluid speed $|\boldsymbol{u}|$, and the arrow indicates gravity.

CRediT authorship contribution statement

Varghese Babu: Writing – review & editing, Writing – original draft, Visualization, Validation, Software, Methodology, Investigation, Formal analysis, Data curation, Conceptualization. **Adrian Kummerländer:** Writing – review & editing, Software, Investigation, Formal analysis, Conceptualization. **Mathias J. Krause:** Writing – review & editing, Supervision, Project administration, Funding acquisition, Conceptualization. **Santosh Ansumali:** Writing – review & editing, Supervision, Methodology. **Dilip Gersappe:** Writing – review & editing, Supervision, Resources, Project administration, Funding acquisition, Conceptualization.

Declaration of generative AI and AI-assisted technologies in the manuscript preparation process

During the preparation of this work the authors used Google-Gemini and Claude-Code for formatting the manuscript and for generating python code involved in plotting the figures. After using this tool/service, the authors reviewed and edited the content as needed and take full responsibility for the content of the published article.

Declaration of competing interest

The authors declare that they have no known competing financial interests or personal relationships that could have appeared to influence the work reported in this paper.

Acknowledgements

DG and VB acknowledge support from the United States Army Corps of Engineers, Engineer Research and Development Center's Cold Regions Research and Engineering Laboratory (ERDC-CRREL, Contract No. W913E524C0009). Any opinions, findings, and conclusions or recommendations expressed in this material are those of the author(s) and do not necessarily reflect the views of the Broad Agency Announcement Program and ERDC-CRREL. The authors would like to thank Stony Brook Research Computing and Cyberinfrastructure and the Institute for Advanced Computational Science at Stony Brook University for access to the high-performance SeaWulf computing system, which was made possible by $1.85M in grants from the National Science Foundation (awards 1531492 and 2215987) and matching funds from the Empire State Development's Division of Science, Technology, and Innovation (NYSTAR) program (contract C210148). We also thank Srikanth Sastry and Pingali Niharika Shankar for valuable discussions.

AK and MK acknowledge funding by the Deutsche Forschungsgemeinschaft (DFG, German Research Foundation) – project number 422374351.

A Methods details.

A.1 Lattice Boltzmann Method

A.1.1 Target equations and volume penalization

The fluid is governed by the incompressible Navier-Stokes equations on the time-dependent fluid domain $\Omega_f(t) = \Omega \setminus \bigcup_k B_k(t)$, where $B_k(t)$ is the region occupied by the rigid body k at time t,

$$\nabla \cdot \mathbf{u} = 0, \tag{6}$$

$$\frac{\partial \mathbf{u}}{\partial t} + \mathbf{u} \cdot \nabla \mathbf{u} = -\frac{\nabla p}{\rho} + \nu \nabla^2 \mathbf{u}, \tag{7}$$

subject to the no-slip condition

$$\mathbf{u} = \mathbf{u}_p \quad \text{on} \partial B_k(t), \tag{8}$$

on every moving body surface, where $\mathbf{u}_p$ is the local velocity of the body. Rather than discretizing Eqs. (6)–(8) directly, we solve a penalized problem on the full, fixed domain Ω,

$$\frac{\partial \mathbf{u}}{\partial t} + \mathbf{u}\cdot\nabla\mathbf{u} = -\frac{\nabla p}{\rho} + \nu\nabla^2\mathbf{u} - \frac{1}{\eta_p}\chi(\mathbf{x},t)\left(\mathbf{u}-\mathbf{u}_p\right), \tag{9}$$

where $\chi(\mathbf{x}, t)$ is the indicator function of the region occupied by the bodies and $\eta_p > 0$ is the penalization parameter. The added term is a Brinkman type volume penalization (Angot et al., 1999), formally the Darcy drag of a porous medium of permeability $K = \nu\eta_p$, although no physical porous medium is modeled here. It vanishes in the fluid and drives the velocity towards $\mathbf{u}_p$ inside the bodies, so that solutions of Eq. (9) converge to the solution of Eqs. (6)–(8) for $\eta_p \to 0$ (Angot et al., 1999). The geometry of the bodies, their motion and their contacts enter only through χ. The same formulation is used in (Kummerländer, Tur, et al., 2026) for the closing contact of oscillating vocal folds and in (Kummerländer, Ito, et al., 2026) for blade-resolved simulations of wind turbine rotors. The discrete counterpart of $1-\chi$ is the porosity field $d(\mathbf{x}, t)$ used throughout this work, with $d = 1$ on fluid nodes, $d = 0$ on solid nodes and a continuous transition between the two across the surface of a body.

A.1.2 Lattice Boltzmann discretization

The Lattice Boltzmann method solves Eqs. (6) and (7) via a discrete in space-time kinetic theory. A discrete velocity set $\mathscr{C} = \{\mathbf{C}_1, \ldots, \mathbf{C}_n\}$ with associated populations $\{f_1, \ldots, f_n\}$ and non-negative weights $\{w_1, \ldots, w_n\}$ is chosen to respect the symmetries required by the fluid flow. Grid spacing Δx and time step Δt are chosen such that particle populations move precisely from one lattice node to an adjacent node along the discrete velocity vectors $\mathbf{C}_i$ in a single time step Δt. The f_i populations are related to density ρ and velocity $\mathbf{v}$ of the fluid at a lattice node as

$$\rho(\mathbf{x},t) = \sum_i^n f_i(\mathbf{x},t)$$

$$\boldsymbol{\rho v}(\mathbf{x},t) = \sum_i^n \mathbf{C}_i f_i(\mathbf{x},t)$$

. The variable f_i's are evolved using the following equation

$$f_i(\mathbf{x}+\mathbf{C}_i\Delta t, t+\Delta t) = f_i(\mathbf{x},t) + \frac{1}{\tau}\left[f_i^{eq}(\rho,\mathbf{v}) - f_i(\mathbf{x}.t)\right] \tag{10}$$

where

$$f_i^{eq}(\rho,\mathbf{v}) = w_i\rho \times \left(1 + \frac{\mathbf{C}_i.\mathbf{v}}{c_s^2} + \frac{(\mathbf{C}_i.\mathbf{v})^2}{2c_s^4} - \frac{\mathbf{v}^2}{2c_s^2}\right)$$

is the equilibrium distribution. Here c_s is a constant with dimension of velocity. The simulation consists of two steps: a collision step where RHS of eq. (10) is calculated at a lattice node and a streaming step where the updated f_i's are moved or streamed to the adjacent lattice node connected by the vector $\mathbf{C}_i$. A Chapman-Enskog analysis, as shown in various standard textbooks (Krüger et al., 2017), recovers Eqs. (6) and (7) with the kinematic viscosity

$$\nu = c_s^2\left(\tau - \frac{1}{2}\right)\frac{\Delta x^2}{\Delta t} \tag{11}$$

so that $\tau > 0.5$ is required for physical viscosities. We use the D3Q19 velocity set, for which mass and momentum are conserved. The penalization term of Eq. (9) is recovered by adding a forcing term to the collision step, as described in Appendix A.3.

For a given physical viscosity and lattice spacing Δx, Eq. (11) links the choice of τ to the timestep Δt. The timestep in turn sets the lattice velocity and thus the Mach number of the simulation. Values of τ close to 1/2 reduce the compressibility error. They require more timesteps and reduce the stability margin of the BGK collision. Larger values of τ increase the compressibility error and the dependence of the boundary representation on τ (Krüger et al., 2017, Ch. 7). The values of τ used in this work are listed in Tables 2 and 3 Their effect on the drag force and on the settling velocities is shown in Appendices B, C and D.

The simulations are set up in physical units and converted to lattice units with the conversion factors $C_L = \Delta x$ for length, $C_t = \Delta t$ for time, $C_u = \Delta x/\Delta t$ for velocity and $C_\rho = \rho_f$ for density. Forces are converted with $C_F = C_\rho C_L^4/C_t^2$. The lattice spacing is given by the particle diameter and the resolution as $\Delta x = d/N_{res}$. The timestep follows from τ and the physical viscosity by Eq. (11) as $\Delta t = c_s^2(\tau - 1/2)\Delta x^2/\nu$. For the hindered settling simulations ($d_{sphere} = 0.35$ mm, $N_{res} = 12$, $\tau = 0.55$, $\nu = 10^{-6}$ m^2/s) this gives $\Delta x = 2.92 \times 10^{-5}$ m and $\Delta t = 1.42 \times 10^{-5}$ s. The terminal velocity of a single sphere $U_t \approx 0.048$ m/s then corresponds to a lattice velocity of 0.023 and a Mach number of Ma ≈ 0.04. The velocities in the hindered settling simulations are smaller than this.

A.2 DEM

First we will discuss the DEM method used in the simulations for particles. We will discuss the contact force between spherical particles of different radii. Since we are using the clump representation for arbitrary shapes, all interactions between rigid bodies can be resolved through interaction between spheres. The force acting between two spheres i and j of radii R_i and R_j is given by a normal component,

$$\mathbf{F}_n = \frac{4}{3}E_{eff}R^{1/2}\delta_{ij}^{3/2}\mathbf{n} - \eta_n\boldsymbol{v}_{n,rel}$$

which is a repulsive force acting when particles overlap. Here E_{eff} is the effective Young's modulus given by

$$E_{\text{eff}} = \frac{1}{\left(\frac{1-\nu_i^2}{E_i} + \frac{1-\nu_j^2}{E_j}\right)}$$

$, R = \frac{R_i R_j}{R_i + R_j}$, $\delta_{ij} = R_i + R_j - |\mathbf{r}_{ij}|$, where $\mathbf{r}_{ij} = \mathbf{r}_i - \mathbf{r}_j$ and $\mathbf{n} = \frac{\mathbf{r}_{ij}}{|\mathbf{r}_{ij}|}$. The second term in the normal interation is the viscous damping term, here $\mathbf{v}_{n,rel} = (\mathbf{v}_j - \mathbf{v}_i) \cdot \mathbf{n}\ \mathbf{n}$, and $\eta_n = -2\sqrt{\frac{5}{6}} \frac{\log(e)}{\sqrt{\pi^2 + (\log(e))^2}} \sqrt{\frac{3}{2} k_{nd} m_{eff}}$, where $k_{nd} = \frac{4}{3} E_{eff} a$ with $a = \sqrt{\delta_{ij} R}, m_{eff} = \frac{M_i M_j}{M_i + M_j}$ and e is the coefficient of restitution.

In addition to this, there is a tangential component,

$$\mathbf{F}_{te} + \mathbf{F}_{t,damp} = \begin{cases} \int_{t_0}^{t} k_t a \mathbf{v}_{t,rel}(\tau) d\tau - \eta_n \mathbf{v}_{t,rel} \\ \quad \text{if} \mathbf{F}_{te} + \mathbf{F}_{t,damp} < \mu_t |\mathbf{F}_n| \\ \mu_t |\mathbf{F}_n| \\ \quad \text{if} \mathbf{F}_{te} + \mathbf{F}_{t,damp} > \mu_t |\mathbf{F}_n| \end{cases} \tag{12}$$

where $\mathbf{v}_{t,rel} = \mathbf{v}_t - (R_i \boldsymbol{\Omega}_i + R_j \boldsymbol{\Omega}_j) \times \mathbf{n}$, $\mathbf{v}_t = \mathbf{v}_r - \mathbf{v}_r \cdot \mathbf{n}\ \mathbf{n}$, $\mathbf{v}_r = \mathbf{v}_j - \mathbf{v}_i$, μ_t is the friction co-efficient, $k_t = 8\left(\frac{2-\nu_i}{G_i} + \frac{2-\nu_j}{G_j}\right)^{-1}$ with $G_i = E_i/(2(1+\nu_i))$. These interactions are implemented in LAMMPS as pair_style granular with hertz/material for normal interaction and tangential mindlin for tangential interaction.

A.3 Fluid-Structure Interaction

In this section we describe how particle motion influences the populations f_i's and how forces acting on the particles are calculated from f_i's.

A.3.1 How f_i's are modified due to particle motion

A given lattice node with $d < 1$ has a velocity $\mathbf{u}_p$ defined by the particle's translational and rotational velocity. In addition to the standard BGK collision Eq. (10), we have to apply the Brinkman penalization as an external force, which is applied to the system through the exact difference scheme of Kupershtokh (Trunk et al., 2021). First we calculate

$$\mathbf{u}^+ = \mathbf{v} + (1-d)[\mathbf{u}_p - \mathbf{v}] \tag{13}$$

and then the populations are modified by

$$S_i = f_i^{eq}(\rho, \mathbf{u}^+) - f_i^{eq}(\rho, \mathbf{v}) \tag{14}$$

with S_i's added to the RHS of Eq. (10) before streaming. The physical velocity is calculated using

$$\mathbf{u}^* = \mathbf{v} + \frac{1}{2}(1-d)[\mathbf{u}_p - \mathbf{v}] \tag{15}$$

as described in (Krüger et al., 2017).

An external body force $\mathbf{F}$ acting on the fluid is applied by the very same construction and simply adds to the shifted velocity,

$$\mathbf{u}^+ = \mathbf{v} + \frac{\Delta t}{\rho}\mathbf{F} + (1-d)[\mathbf{u}_p - \mathbf{v}], \tag{16}$$

so that the body force and the penalization are realized by a single exact difference step, with the corresponding term $\Delta t\, \mathbf{F}/(2\rho)$ added to Eq. (15). In the hindered settling simulations, $\mathbf{F}$ is the compensating force of Sec. 4.1, which keeps the mean velocity of the fluid at zero.

Comparing this with the penalized momentum equation Eq. (9), the scheme relaxes the local velocity towards $\mathbf{u}_p$ by the fraction $(1-d)$ in every timestep, i.e. the discrete penalization parameter is $\eta_p = \Delta t/(1-d)$ and the corresponding local permeability is $K = \nu\eta_p$. In the fully fluid limit $d = 1$ the forcing vanishes and the scheme reduces to standard BGK, while inside a body $d = 0$ and the penalization is at its strongest. The attainable penalization is thus bounded by the timestep rather than chosen freely, so that at a fixed resolution the residual slip, and hence the position of the effective hydrodynamic surface, retains a weak dependence on τ. This is the origin of the τ dependence reported in Appendix B and Appendix D.

A.3.2 How forces on particles are calculated from f_i's

We use the Galilean invariant momentum exchange formulation from (Wen et al., 2014), where the hydrodynamic force acting on a given particle is calculated by

$$\mathbf{F}^H(t) = -\sum_{\mathbf{x} \in B} \sum_{i=1}^{q} \left[(\mathbf{C}_i - \mathbf{u}_p) f_i(\mathbf{x} + \mathbf{C}_i, t) + (\mathbf{C}_i + \mathbf{u}_p) f_{\tilde{i}}(\mathbf{x}, t)\right] \tag{17}$$

where $\tilde{i}$ is the direction opposite to i. The sum is restricted to the lattice links that cross the fluid-solid interface, i.e. to the nodes $\mathbf{x}$ with $d < 1$ that belong to the particle and whose neighbour $\mathbf{x} + \mathbf{C}_i$ is a pure fluid node with $d = 1$. Nodes in the interior of a particle, which have no fluid neighbour, do not contribute. The corresponding torque about the particle pivot $\mathbf{x}_p$ follows as

$$\mathbf{T}^{\mathrm{H}}(t) = \sum_{\mathbf{x}\in B} (\mathbf{x} - \mathbf{x}_{\mathrm{p}}) \times \mathbf{F}^{\mathrm{H}}(\mathbf{x}, t), \tag{18}$$

where $\mathbf{F}^{\mathrm{H}}(\mathbf{x}, t)$ is the per-node contribution to Eq. (17). For the periodic directions of the domain, the lever arm $\mathbf{x} - \mathbf{x}_{\mathrm{p}}$ is taken with respect to the nearest periodic image of the pivot, i.e. each component is shifted by the corresponding domain length whenever it exceeds half of it. Without this minimum image convention, a particle straddling a periodic boundary would be assigned lever arms of nearly the domain length for the nodes on the far side.

A.3.3 Representation of a particle in the fluid

We initialize a reference lattice, whose dimensions bound the object we would like to represent, with a porosity field representing the.stl file using STLreader capability of OpenLB. The reference lattice is resolved at half the spacing of the fluid lattice and its nodes are set to 0 or 1 depending on whether they fall inside or outside the surface mesh, so that the reference porosity is an exact voxelization of the given geometry. The same voxelization provides the volume, the mass and the inertia tensor of the body, which are passed to LAMMPS through its infile feature, so that the fluid and the DEM side use a consistent description of the rigid body.

Given a pivot to place the particle (taken to be its center of mass) and the orientation about the pivot, we can map a given lattice node in our domain to a point in the reference lattice and therefore use the predefined porosity field to embed the particle in our lattice. The porosity assigned to a node of the fluid lattice is the average of the reference porosity over the mapped node and its 26 neighbours of the D3Q27 stencil in the reference lattice. This average is a discrete approximation of the porosity profile used in Kummerländer, Tur, et al. (2026), which is defined by the signed distance ϕ to the surface of the body, positive in the fluid,

$$d(\mathbf{x}, t) = \begin{cases} 0 & \text{if} \phi(\mathbf{x}, t) \leq -\epsilon_h/2, \\ \dfrac{1}{2} + \dfrac{\phi(\mathbf{x}, t)}{\epsilon_h} & \text{if} |\phi(\mathbf{x}, t)| < \epsilon_h/2, \\ 1 & \text{if} \phi(\mathbf{x}, t) \geq \epsilon_h/2, \end{cases} \tag{19}$$

so that the surface of the body is the level set $d = 1/2$. For a surface that is flat on the scale of Δx, the average over the D3Q27 stencil yields this linear profile with a transition width of about three reference cells, that is $\epsilon_h \approx 1.5\,\Delta x$. The interface between fluid and solid thus spans one to two cells of the fluid lattice. As discussed in Kummerländer, Tur, et al. (2026), higher order profiles offer no advantage at this width, and the transition introduces a truncation error of order ϵ_h near the interface. This error appears as the dependence of the settling velocities on N_{res} and τ in Appendices C and D. The stencil is aligned with the reference lattice and rotates with the body. The faces of a cube therefore always see the same profile, independent of the orientation of the cube relative to the fluid lattice. The mapping uses the same minimum image convention as above, so that a particle whose support crosses a periodic boundary is embedded as one body.

The solid velocity entering the forcing follows from the rigid body kinematics of the body k covering the node,

$$\mathbf{u}_{\mathrm{p}}(\mathbf{x}, t) = \mathbf{v}_{\mathrm{k}}(t) + \boldsymbol{\omega}_{\mathrm{k}}(t) \times (\mathbf{x} - \mathbf{x}_{\mathrm{k}}(t)), \tag{20}$$

for center of mass $\mathbf{x}_{\mathrm{k}}$, translational velocity $\mathbf{v}_{\mathrm{k}}$ and angular velocity $\boldsymbol{\omega}_{\mathrm{k}}$.

During the motion of particles in the simulation, this procedure is repeated to keep track of the porosity field. Updating the porosity field after a displacement or a rotation of a body does not require a re-evaluation of all the nodes of the domain. Between two timesteps the surface of a body may not travel further than the distance between adjacent nodes, so that only the nodes currently covered by a body and a surrounding growth layer have to be revisited. The cost of the geometry update, like that of the force evaluation, is therefore proportional to the surface and not to the volume of the bodies. The porosity embedding and the surface force integration are implemented as platform-transparent operators in OpenLB and are executed on the GPU as described in (Kummerländer et al., 2026a, 2026b).

B Drag force on cubic array of spheres

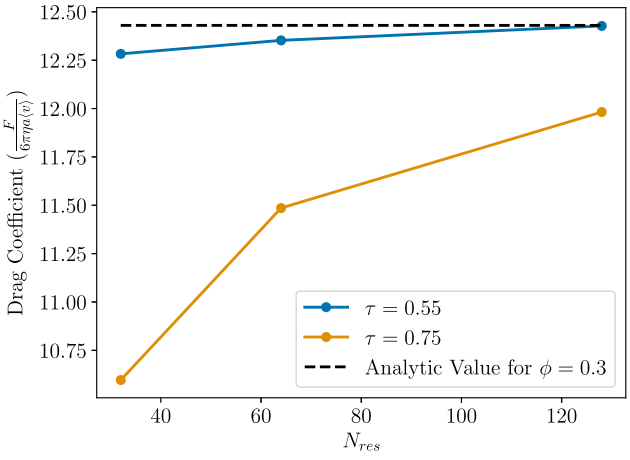


Fig. A.1. Drag force for different τ and N_{res} at $\phi = 0.3$.

In this section we describe the validation associated with calculating the drag force on a cubic array of spheres. For a packing fraction $\phi = 0.3$ we run the simulation for different values of τ and N_{res}. The results are shown in Fig. A.1, where we observe a convergence to thee analytical value. Since the force acting on the sphere at steady state is equal to the applied force to the fluid for all values of τ, the average velocity is the value that changes as we change the parameter. Therefore, we observe a higher velocity than the analytical prediction for higher values of τ, which we observe also in the single sphere settling.

C Sphere settling velocity

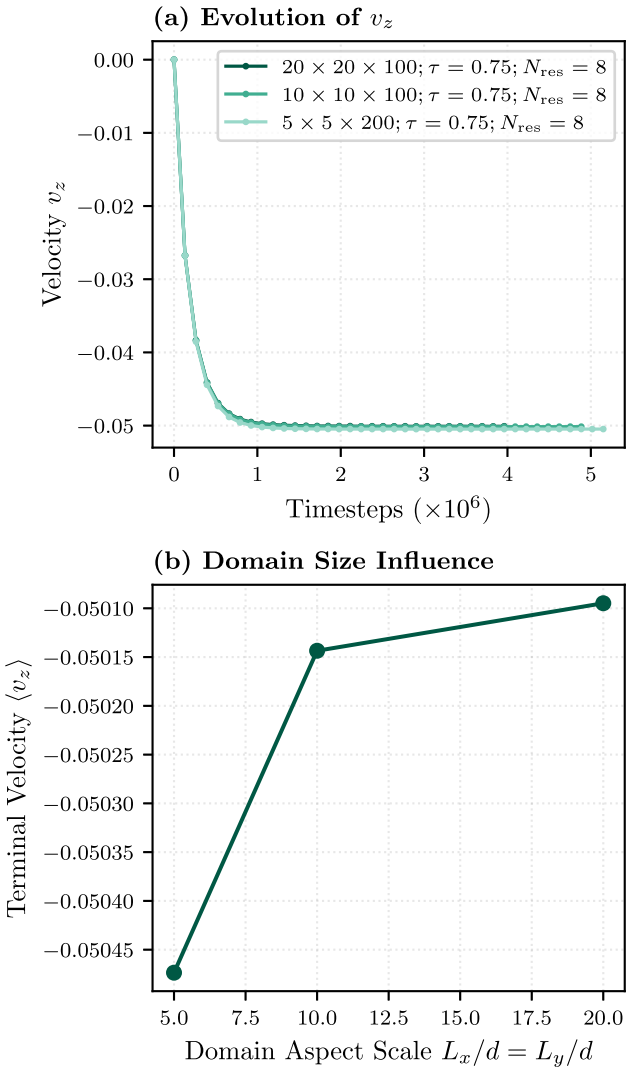


Fig. A.2. For $N_{\text{res}} = 8$, i.e the diameter is resolved upto 8 l.u's.

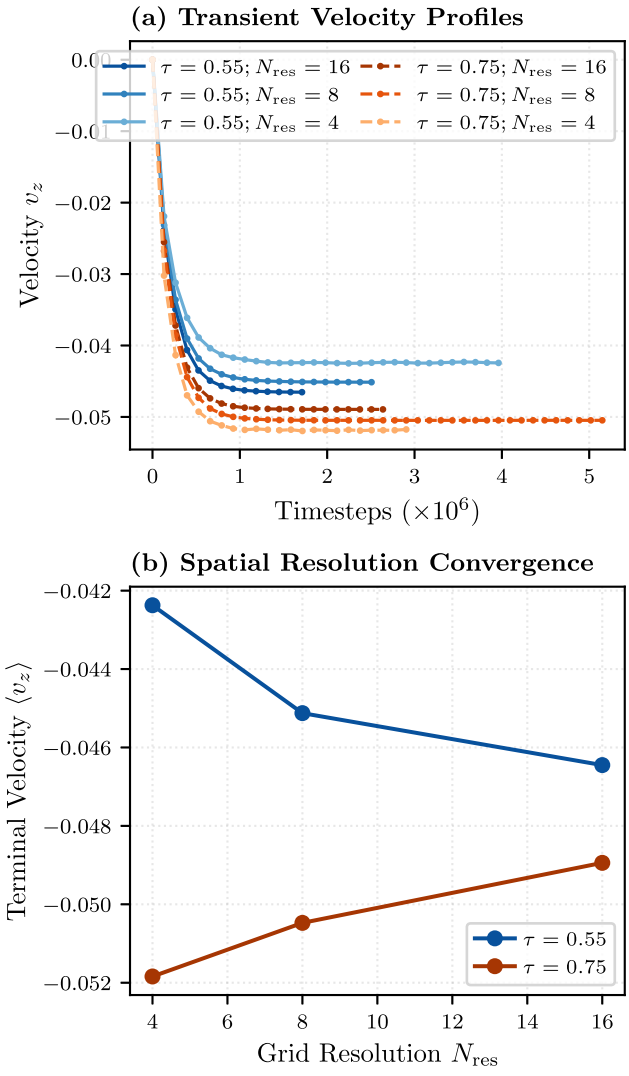


Fig. A.3. Settling velocity of sphere as one increases the resolution with which a diameter is resolved for two different τ values.

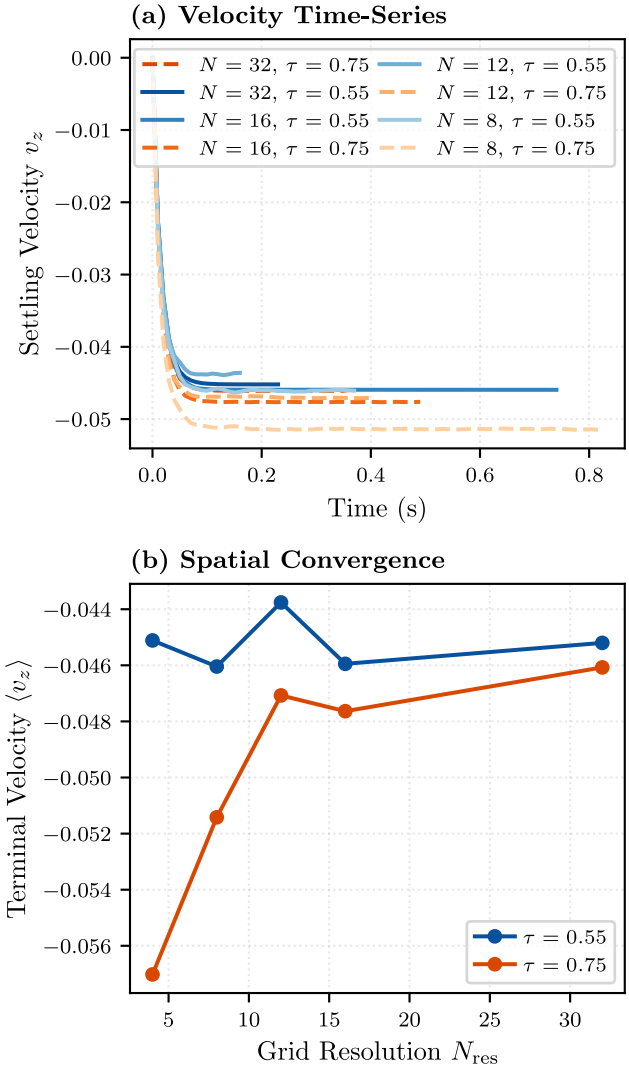


Fig. A.4. Terminal velocities of a single cube for different resolutions N_{res} and for two different relaxation times τ.

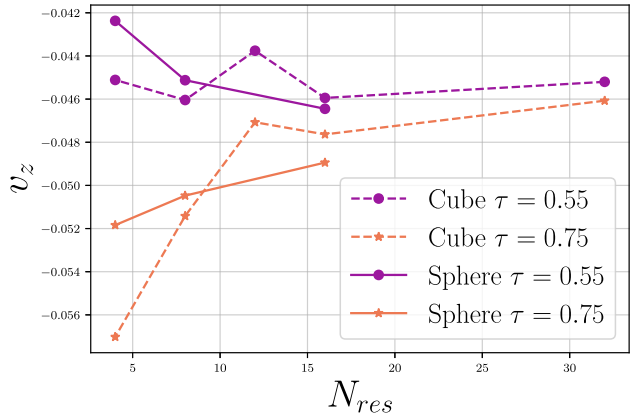


Fig. A.5. Comparison of cube and sphere settling velocity for different resolutions and relaxation times.

In this section we describe sphere settling simulations. We will calibrate the system by comparing the terminal velocity of the sphere with a known ground truth. The system under study has $d = 0.35 \times 10^{-3}$ m diameter, $\rho_{\text{p}} = 2500$ kg/m^3, $\rho_{\text{f}} = 1000$ kg/m^3 and $\mu = 10^{-3}$ Pa s (same as the one used in Rettinger and Rüde (2017b)). The terminal velocity of a single particle is taken to be ≈ 0.048 m/s. We need to study the influence of τ, N_{res}, on the numerical terminal velocity. First, we study different domain sizes as multiples of the diameter of the sphere to ascertain the dependence of domain size on the terminal velocity. For the simulation, we use bounceback boundary condition for the top and bottom walls, a pressure boundary condition

for the side walls as implemented in interpolatedPressureBoundary in OpenLB. As shown in Fig. A.2, the effect of the domain walls only changes the terminal velocity by less than 1%. Therefore for further studies we will use the $5 \times 5 \times 200$ box size.

In Fig. A.3 we plot the variation of v_z as we increase the resolution of the sphere diameter for two relaxation times τ. As seen in the graph, as we increase the resolution of the system, the value seems to converge to a value around the expected value of around ~ 0.048. As resolution is increased, the effect of relaxation time τ reduces, indicating that the simulation is converging.

D Cube Settling Velocity

Similar to the preceding sphere study, we study the effect of τ and N_{res} on the cube settling velocity. In Fig. A.4, we show the dependence of the cube velocity on different parameters. Again, we observe a convergence to a value close to ~ -0.046 m/s. This is close to, but faster than what is predicted from empirical relations - Haider's formula Haider and Levenspiel (1989) predicts ~ 0.0437 m/s. From existing literature Marquardt et al. (2024a), Kundu et al. (2025), Seyed-Ahmadi and Wachs (2021) we expect the cube to settle slower than the sphere. However, we observe that the sphere and the cube terminal velocities are close to each other as shown in Fig. A.5.

E Comparison with Seyed-Ahmadi and Wachs (2021)

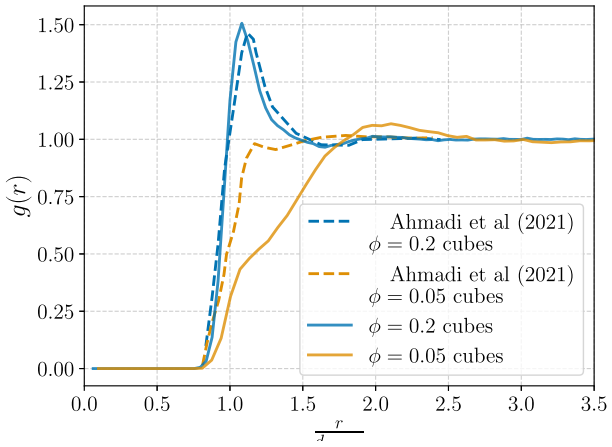


Fig. A.6. Comparison with Seyed-Ahmadi and Wachs (2021).

We compare the radial distribution function obtained for cubes from Seyed-Ahmadi and Wachs (2021) at two different packing fractions as shown in Fig. A.6. Although, their simulation is at a higher Re than ours, we observe that at higher packing fraction, the local structure is very similar. However, at lower packing fractions, there is more clustering for the higher Re case. We also note the that RDF for $\phi = 0.05$ from Seyed-Ahmadi and Wachs (2021) and RDF for $\phi = 0.1$ from Fig. 7 for cubes is quantitatively very similar.

F Lubrication force between the particles

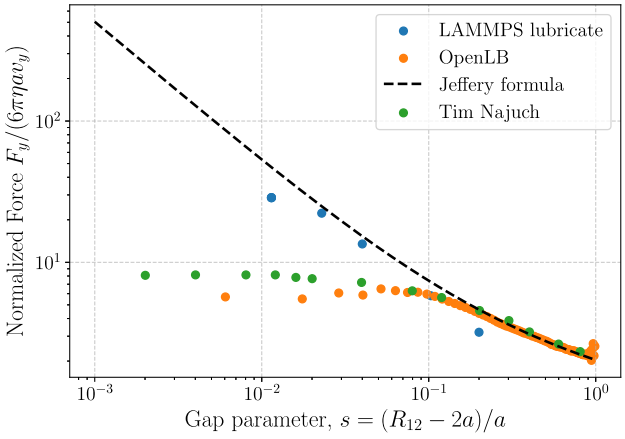


Fig. A.7. The force acting on a sphere compared with its stokes drag for two sphere approaching each other along the y direction.

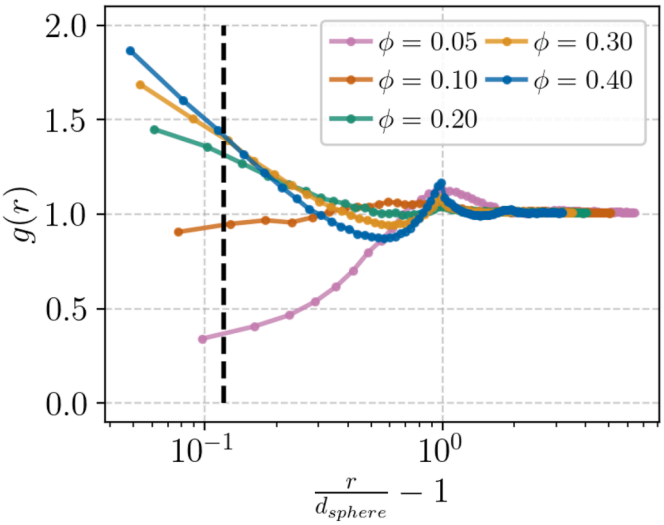


Fig. A.8. RDF of spheres. The black dashed line shows the gap below which lubrication forces are underestimated.

As discussed in Ladd (1994a), Rettinger and Rüde (2017b), Najuch (2019), Ten Cate et al. (2002) there is a repulsive force that acts between two spheres as they come close to each other. This is due to the fluid getting squeezed out of the gap between the two spheres. Numerical simulation by Najuch (2019) show that the partially saturated method underestimates the repulsion between the two spheres approaching each other, necessitating an addition of a lubricating force. As shown in Fig. A.7, LBM without lubrication captures the repulsive force accurately to about a gap of about $\sim 0.12 \times a$. Fig. A.8 shows the RDF of spheres at various packing fractions, along with a line indicating the gap below which forces are not accurate. The spheres that are in contact at higher packing fractions may not occur if lubrication forces are present in the system. Lubrication force correction is applied by calculating the error with the analytical solution (Najuch, 2019, Nguyen and Ladd). There is an implementation of lubrication force between spheres in LAMMPS called fix lubricate. We have shown the magnitude of this force as the spheres approach each other in FIg. A.7. We are in the process of implementing this in our code, but as pointed out, we need to account for the challenge of the small step required as well as the subgrid resolution.

G Hindered Settling of Spheres and Cubes

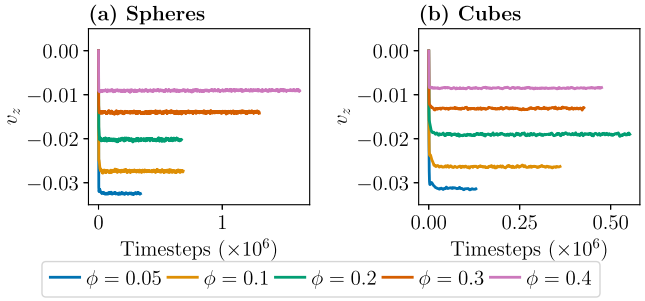


Fig. A.9. Vertical velocity component of sphere and cubes at different packing fractions.

In this section, we present the evolution of settling velocity for bulk suspension at different packing fraction. The results correspond to Fig. 5. We observe that cube always settles slower than sphere at all packing fractions. However, when compared to Marquardt et al. (2024a) reports a 25% difference between the velocities of cubes and spheres, while in our system the difference settling velocities is $\sim$ 6%.

Voxellization error

The volume of the voxelized cube is lower than d_{cube}^3 (by 5%). Hence, while we choose the domain size as described earlier, actual packing fraction simulated (solid nodes/liquid nodes) is lower than the prescribed one. Then the settling velocity will be larger than the value at the correct packing fraction, which might be reason why we find the difference in settling velocity between cubes and spheres to be lower than reported literature value.

H Validation of clump representation

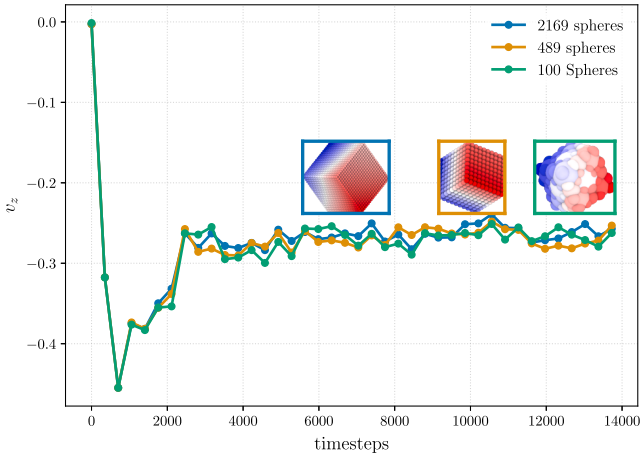


Fig. A.10. Evolution of v_z for hindered settling with two different "clump" representation of cube with 2169, 489 spheres and 100 spheres respectively. The corresponding clumps are shown in the inset.

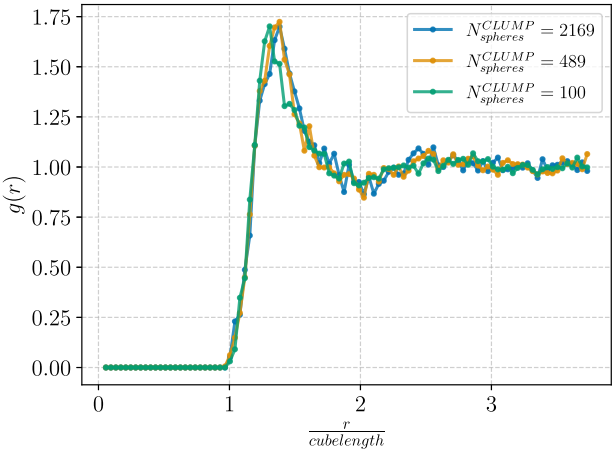


Fig. A.11. RDF for different clump representation.

In this section we present a validation test for clump representation. We perform a hindered settling of 125 cubes. The two representation are shown in the insets. The 100 sphere representation is created using the Angelidakis et al. (2021) library while the 489 and 2169 sphere representations are created by placing spheres in a grid on the cube surfaces. As shown in Fig. A.10, v_z evolves similarly for both systems. We compute the RDF for cubes in hindered settling for the validation case discussed in Appendix H and is shown in Fig. A.11. This shows that different clump representations quantitatively generate similar structures.

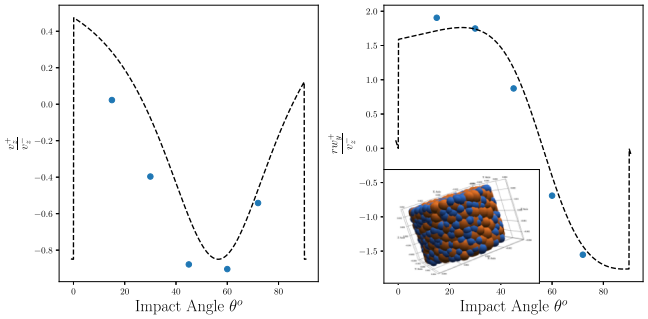


Fig. A.12. Comparison of analytical solution of rebound velocity v_z^+ and angular velocity w_y^+ with numerical result with a clump representation of the cylinder.

Cylinder-wall impact

Following Marquardt and Krause (2024), Trunk et al. (2021), we compare the numerical rebound velocity with analytical solution for a cylinder impacting a wall at an angle θ. The analytical solution is given by

$$\omega_y^+ = \frac{mv_z^-(1+e)r\cos(\alpha+\theta)}{I_{yy} + mr^2\cos^2(\alpha+\theta)}$$

$$v_z^+ = \omega_y^+ r\cos(\alpha+\theta) - ev_z^-.$$

where I_{yy} is the moment of inertia around y axis, e is the coefficient of restitution, m is the mass, $r = \sqrt{R^2 + \frac{1}{4}H^2}$ is distance from the point of impact to the center of mass, α is the angle the line connecting the point of impact with center of mass makes with the base of the cylinder and θ is the impact angle which is the angle the base of the cylinder makes with horizontal wall.

In Fig. A.12 we shown the comparison with numerical results. The clump representation of the cylinder is made of 600 spheres and is shown in the inset. As expected, clump representation introduces errors, however overall agreement is reasonable. Experimenting with different clump representations could improve the agreement with the analytical solution.

References

Ahmadian, M. H., & Zheng, W. (2024). Simulating the fluid–solid interaction of irregularly shaped particles using the LBM-DEM coupling method. *Computers and Geotechnics, 171*, Article 106395. https://doi.org/10.1016/j.compgeo.2024.106395. URL: https://linkinghub.elsevier.com/retrieve/pii/S0266352X24003318.

Angelidakis, V., Nadimi, S., Otsubo, M., & Utili, S. (2021). CLUMP: A code Library to generate universal multi-sphere particles. *SoftwareX, 15*, Article 100735. https://doi.org/10.1016/j.softx.2021.100735. URL: https://www.sciencedirect.com/science/article/pii/S2352711021000704.

Angot, P., Bruneau, C. H., & Fabrie, P. (1999). A penalization method to take into account obstacles in incompressible viscous flows. *Numerische Mathematik, 81*, 497–520. https://doi.org/10.1007/s002110050401

Batchelor, G. K. (1972). Sedimentation in a dilute dispersion of spheres. *Journal of Fluid Mechanics, 52*, 245–268. https://doi.org/10.1017/S0022112072001399

Bauer, M., Eibl, S., Godenschwager, C., Kohl, N., Kuron, M., Rettinger, C., Schornbaum, F., Schwarzmeier, C., Thönnes, D., Köstler, H., & Rüde, U. (2021). waLBerla: A block-structured high-performance framework for multiphysics simulations. *Computers &Mathematics with Applications, 81*, 478–501. https://doi.org/10.1016/j.camwa.2020.01.007

Blais, B., Barbeau, L., Bibeau, V., Gauvin, S., Geitani, T. E., Golshan, S., Kamble, R., Mirakhori, G., & Chaouki, J. (2020). Lethe: An open-source parallel high-order adaptative CFD solver for incompressible flows. *SoftwareX, 12*, Article 100579. https://doi.org/10.1016/j.softx.2020.100579

Capozza, R., & Hanley, K. (2021). A hierarchical, spherical harmonic-based approach to simulate abradable, irregularly shaped particles in DEM. *Powder Technology, 378*, 528–537. https://doi.org/10.1016/j.powtec.2020.10.015

Chong, Y. S., Ratkowsky, D. A., & Epstein, N. (1979). Effect of particle shape on hindered settling in creeping flow. *Powder Technology*. https://doi.org/10.1016/0032-5910(79)85025-1

Climent, E., & Maxey, M. R. (2003). Numerical simulations of random suspensions at finite Reynolds numbers. *International Journal of Multiphase Flow*. https://doi.org/10.1016/s0301-9322(03)00016-8

Cundall, P. A., & Strack, O. D. L. (1979). A discrete numerical model for granular assemblies. *Géotechnique, 29*, 47–65. https://doi.org/10.1680/geot.1979.29.1.47, 10.1680/geot.1979.29.1.47.

Eibl, S. (2021). *Modular and extensible software architecture for particle dynamics*. Friedrich-Alexander-Universitaet Erlangen-Nuernberg (Germany).

Fareed, B., Nadeem, M., Ullah, A., Molina, J. J., Yamamoto, R., Chamorro, L. P., & Hamid, A. (2026). Collective sedimentation of symmetric nonspherical particles in stokes flow. *Physical Review Fluids, 11*, Article 054305. https://doi.org/10.1103/441b-p5mv

Fluent, A. (2023). *Ansys fluent theory guide* (No Title).

Fornari, W., Picano, F., & Brandt, L. (2016). Sedimentation of finite-size spheres in quiescent and turbulent environments. *Journal of Fluid Mechanics, 788*, 640–669. https://doi.org/10.1017/jfm.2015.698

Garside, J., & Al-Dibouni, M. R. (1977). Velocity-voidage relationships for fluidization and sedimentation in solid-liquid systems. *Industrial &engineering chemistry process design and development, 16*, 206–214.

Goniva, C., Kloss, C., Deen, N. G., Kuipers, J. A., & Pirker, S. (2012). Influence of rolling friction on single spout fluidized bed simulation. *Particuology, 10*, 582–591.

Guazzelli, E. (2001). Evolution of particle-velocity correlations in sedimentation. *Physics of Fluids, 13*, 1537–1540.

Guazzelli, É., & Hinch, J. (2011). Fluctuations and instability in sedimentation. *Annual Review of Fluid Mechanics, 43*, 97–116. https://doi.org/10.1146/annurev-fluid-122109-160736

Haider, A., & Levenspiel, O. (1989). Drag coefficient and terminal velocity of spherical and nonspherical particles. *Powder Technology*. https://doi.org/10.1016/0032-5910(89)80008-7

Hasimoto, H. (1959). On the periodic fundamental solutions of the stokes equations and their application to viscous flow past a cubic array of spheres. *Journal of Fluid Mechanics, 5*, 317–328.

Kloss, C., Goniva, C., Hager, A., Amberger, S., & Pirker, S. (2012). Models, algorithms and validation for opensource dem and cfd–dem. Progress in computational fluid dynamics. *An International Journal, 12*, 140–152.

Krause, M., Kummerländer, A., Avis, S., Kusumaatmaja, H., Dapelo, D., Klemens, F., Gaedtke, M., Hafen, N., Mink, A., Trunk, R., Marquardt, J., Maier, M., Haussmann, M., & Simonis, S. (2021). OpenLB–Open source lattice Boltzmann code. *Computers &Mathematics with Applications, 81*, 258–288. https://doi.org/10.1016/j.camwa.2020.04.033. URL: http://www.sciencedirect.com/science/article/pii/S0898122120301875.

Krause, M. J., Klemens, F., Henn, T., Trunk, R., & Nirschl, H. (2017). Particle flow simulations with homogenised lattice Boltzmann methods. *Particuology, 34*, 1–13. https://doi.org/10.1016/j.partic.2016.11.001. URL: https://linkinghub.elsevier.com/retrieve/pii/S167420011730041X.

Krüger, T., Kusumaatmaja, H., Kuzmin, A., Shardt, O., Silva, G., & Viggen, E. M. (2017). The lattice boltzmann method: Principles and practice. In *Graduate texts in physics*. Cham: Springer International Publishing https://doi.org/10.1007/978-3-319-44649-3.

Kummerländer, A., Ito, S., Schecher, M., Dapelo, D., Simonis, S., Krause, M. J., & Bukreev, F. (2026). Efficient wall-modelled large eddy simulation of rotors using homogenized lattice boltzmann methods. *International Journal of Numerical Methods for Heat and Fluid Flow*, 1–25. https://doi.org/10.1108/HFF-09-2025-0724, 10.1108/HFF-09-2025-0724.

Kummerländer, A., Tur, B., Haase, M., Bukreev, F., Döllinger, M., Krause, M. J., & Kniesburges, S. (2026). Efficient fluid structure interaction simulation of vocal fold oscillations using a homogenized lattice boltzmann method. *Computer Methods in Applied Mechanics and Engineering, 457*, Article 119009. https://doi.org/10.1016/j.cma.2026.119009. URL: https://www.sciencedirect.com/science/article/pii/S0045782526002823.

Kundu, D., Usabiaga, F. B., & Ellero, M. (2025). Settling dynamics of Non-Brownian suspension of spherical and cubic particles in Stokes flow. http://arxiv.org/abs/2501.08091. arXiv:2501.08091 [physics].

Kwon, S. J., Park, Y. G., Quyen, L. D., Lee, I. C., & Choi, J. M. (2025). Experimental investigation of settling velocity for cuboidal microplastic. *Applied Ocean Research, 161*, Article 104693. https://doi.org/10.1016/j.apor.2025.104693. URL: https://www.sciencedirect.com/science/article/pii/S0141118725002792.

Ladd, A. J. (1988). Hydrodynamic interactions in a suspension of spherical particles. *The Journal of chemical physics, 88*, 5051–5063.

Ladd, A. J. C. (1994a). Numerical simulations of particulate suspensions via a discretized Boltzmann equation. Part 1. Theoretical foundation. *Journal of Fluid Mechanics, 271*, 285–309. https://doi.org/10.1017/S0022112094001771. URL: https://www.cambridge.org/core/product/identifier/S0022112094001771/type/journal_article.

Ladd, A. J. C. (1994b). Numerical simulations of particulate suspensions via a discretized Boltzmann equation. Part 2. Numerical results. *Journal of Fluid Mechanics, 271*, 311–339. https://doi.org/10.1017/S0022112094001783. URL: https://www.cambridge.org/core/product/identifier/S0022112094001783/type/journal_article.

Ladd, A. J. C. (1996). Hydrodynamic screening in sedimenting suspensions of Non-Brownian spheres. *Physical Review Letters, 76*, 1392–1395. https://doi.org/10.1103/PhysRevLett.76.1392

Ladd, A. J. C. (1997). Sedimentation of homogeneous suspensions of Non-Brownian spheres. *Physics of Fluids, 9*, 491–499. https://doi.org/10.1063/1.869212

Ladd, A. J. C. (2002). Effects of container walls on the velocity fluctuations of sedimenting spheres. *Physical Review Letters, 88*, Article 048301. https://doi.org/10.1103/PhysRevLett.88.048301

Latt, J., Malaspinas, O., Kontaxakis, D., Parmigiani, A., Lagrava, D., Brogi, F., Belgacem, M. B., Thorimbert, Y., Leclaire, S., Li, S., Marson, F., Lemus, J., Kotsalos, C., Conradin, R., Coreixas, C., Petkantchin, R., Raynaud, F., Beny, J., & Chopard, B. (2021). Palabos: Parallel lattice Boltzmann Solver. *Computers &*

Mathematics with Applications, 81, 334–350. https://doi.org/10.1016/j.camwa.2020.03.022

Li, X., Hunt, M. L., & Colonius, T. (2012). A contact model for normal immersed collisions between a particle and a wall. *Journal of Fluid Mechanics, 691*, 123–145. https://doi.org/10.1017/jfm.2011.461. URL: https://www.cambridge.org/core/product/identifier/S0022112011004617/type/journal_article.

Lu, G., Third, J. R., & Müller, C. R. (2015). Discrete element models for non-spherical particle systems: From theoretical developments to applications. *Chemical Engineering Science*. https://doi.org/10.1016/j.ces.2014.11.050

Maggio-Aprile, R., Rambosson, M., Coreixas, C., & Latt, J. (2025). *LEDDS: Portable LBM-DEM simulations on GPUs*. https://doi.org/10.48550/ARXIV.2512.04997

Marquardt, J. E., Hafen, N., & Krause, M. J. (2024a). A novel model for direct numerical simulation of suspension dynamics with arbitrarily shaped convex particles. *Computer Physics Communications, 304*, Article 109321. https://doi.org/10.1016/j.cpc.2024.109321. URL: https://www.sciencedirect.com/science/article/pii/S0010465524002443.

Marquardt, J. E., Hafen, N., & Krause, M. J. (2024b). A novel particle decomposition scheme to improve parallel performance of fully resolved particulate flow simulations. *Journal of Computational Science, 78*, Article 102263. https://doi.org/10.1016/j.jocs.2024.102263. URL: https://www.sciencedirect.com/science/article/pii/S1877750324000565.

Marquardt, J. E., & Krause, M. J. (2024). A review of the homogenized lattice Boltzmann method for particulate flow simulations: From fundamentals to applications. *Powders, 3*, 500–530. URL: https://www.mdpi.com/2674-0516/3/4/27, 10.3390/powders3040027. number: 4.

Marquardt, J. E., Römer, U. J., Nirschl, H., & Krause, M. J. (2023). A discrete contact model for complex arbitrary-shaped convex geometries. *Particuology, 80*, 180–191. https://doi.org/10.1016/j.partic.2022.12.005. URL: https://linkinghub.elsevier.com/retrieve/pii/S1674200122002784.

Moriche, M., García-Villalba, M., & Uhlmann, M. (2026). Particle-resolved simulations of settling particles: A methodology for long time-integration intervals. *Acta Mechanica*. https://doi.org/10.1007/s00707-026-04653-1

Najuch, T. (2019). *Simulation of dense suspensions with discrete element method and a coupled lattice boltzmann method*. Ph.D. thesis.

Najuch, T., & Sun, J. (2019). Analysis of two partially-saturated-cell methods for lattice Boltzmann simulation of granular suspension rheology. *Computers &Fluids, 189*, 1–12. https://doi.org/10.1016/j.compfluid.2019.05.004

Nguyen, N.Q., Ladd, A.J.C., . Lubrication corrections for lattice-Boltzmann simulations of particle suspensions. Physical Review E 66, 046708. URL: https://link.aps.org/doi/10.1103/PhysRevE.66.046708, doi:10.1103/PhysRevE.66.046708.

Noble, D. R., & Torczynski, J. R. (1998). A lattice-Boltzmann method for partially saturated computational cells. *International Journal of Modern Physics C, 9*, 1189–1201.

Paul, N., Biggs, S., Shiels, J., Hammond, R. B., Edmondson, M., Maxwell, L., Harbottle, D., & Hunter, T. N. (2017). Influence of shape and surface charge on the sedimentation of spheroidal, cubic and rectangular cuboid particles. *Powder Technology, 322*, 75–83. https://doi.org/10.1016/j.powtec.2017.09.002. URL: https://linkinghub.elsevier.com/retrieve/pii/S0032591017307234.

Rettinger, C., & Rüde, U. (2017a). A comparative study of fluid-particle coupling methods for fully resolved lattice Boltzmann simulations. *Computers &Fluids, 154*, 74–89. https://doi.org/10.1016/j.compfluid.2017.05.033. URL: http://arxiv.org/abs/1702.04910. arXiv:1702.04910 [cs].

Rettinger, C., & Rüde, U. (2017b). A coupled lattice boltzmann method and discrete element method for discrete particle simulations of particulate flows. http://arxiv.org/abs/1711.00336, 10.48550/arXiv.1711.00336. arXiv:1711.00336 [cs].

Richardson, J. F., & Zaki, W. N. (1954). The sedimentation of a suspension of uniform spheres under conditions of viscous flow. *Chemical Engineering Science, 3*, 65–73. https://doi.org/10.1016/0009-2509(54)85015-9. URL: https://www.sciencedirect.com/science/article/pii/0009250954850159.

Sangani, A. S., & Acrivos, A. (1982). Slow flow through a periodic array of spheres. *International Journal of Multiphase Flow, 8*, 343–360.

Segrč, P. N., Herbolzheimer, E., & Chaikin, P. M. (1997). Long-Range correlations in sedimentation. *Physical Review Letters, 79*, 2574–2577. URL: https://link.aps.org/doi/10.1103/PhysRevLett.79.2574, 10.1103/PhysRevLett.79.2574.

Segre, P. N., Liu, F., Umbanhowar, P., & Weitz, D. A. (2001). An effective gravitational temperature for sedimentation. *Nature, 409*, 594–597.

Seil, P., & Pirker, S. (2016). Lbdemcoupling: Open-source power for fluid-particle systems. In *International conference on discrete element methods* (pp. 679–686). Springer.

Seyed-Ahmadi, A., & Wachs, A. (2021). Sedimentation of inertial monodisperse suspensions of cubes and spheres. *Physical Review Fluids, 6*, Article 044306. https://doi.org/10.1103/PhysRevFluids.6.044306. URL: https://link.aps.org/doi/10.1103/PhysRevFluids.6.044306.

Smilauer, V., Angelidakis, V., Catalano, E., Caulk, R., Chareyre, B., Chevremont, W., Dorofeenko, S., Duriez, J., Dyck, N., Elias, J., et al. (2023). *Yade documentation*. arXiv preprint arXiv:2301.00611.

Studeník, O., Isoz, M., Kotouč Šourek, M., & Kočí, P. (2024). OpenHFDIB-DEM: An extension to OpenFOAM for CFD-DEM simulations with arbitrary particle shapes. *SoftwareX, 27*, Article 101871. https://doi.org/10.1016/j.softx.2024.101871

Syamlal, M., Rogers, W., & Obrien, T. J. (1993). *MFIX documentation theory guide*. WV (United States): USDOE Morgantown Energy Technology Center. Technical Report.

Ten Cate, A., Nieuwstad, C. H., Derksen, J. J., & Van Den Akker, H. E. A. (2002). Particle imaging velocimetry experiments and lattice-Boltzmann simulations on a single sphere settling under gravity. *Physics of Fluids, 14*, 4012–4025. https://doi.org/10.1063/1.1512918. URL: https://pubs.aip.org/pof/article/14/11/4012/1008754/Particle-imaging-velocimetry-experiments-and.

Thompson, A. P., Aktulga, H. M., Berger, R., Bolintineanu, D. S., Brown, W. M., Crozier, P. S., in 't Veld, P. J., Kohlmeyer, A., Moore, S. G., Nguyen, T. D., Shan, R., Stevens, M. J., Tranchida, J., Trott, C., & Plimpton, S. J. (2022). LAMMPS - A flexible simulation tool for particle-based materials modeling at the atomic, meso, and continuum scales. *Computer Physics Communications, 271*, Article 108171. https://doi.org/10.1016/j.cpc.2021.108171. URL: https://www.sciencedirect.com/science/article/pii/S0010465521002836.

Trunk, R., Weckerle, T., Hafen, N., Thäter, G., Nirschl, H., & Krause, M. J. (2021). Revisiting the homogenized lattice Boltzmann method with applications on particulate flows. *Computation, 9*, 11. https://doi.org/10.3390/computation9020011. URL: https://www.mdpi.com/2079-3197/9/2/11.

Turk, G., & Levoy, M. (1994). Zippered polygon meshes from range images. In *Proceedings of the 21st annual conference on computer graphics and interactive techniques* (pp. 311–318). New York, NY, USA: ACM. https://doi.org/10.1145/192161.192241.

Uhlmann, M., & Doychev, T. (2014). Sedimentation of a dilute suspension of rigid spheres at intermediate Galileo numbers: The effect of clustering upon the particle motion. *Journal of Fluid Mechanics, 752*, 310–348. https://doi.org/10.1017/jfm.2014.330. arXiv:1406.1667.

Weller, H. G., Tabor, G., Jasak, H., & Fureby, C. (1998). A tensorial approach to computational continuum mechanics using object-oriented techniques. *Computers in Physics, 12*, 620–631.

Wen, B., Zhang, C., Tu, Y., Wang, C., & Fang, H. (2014). Galilean invariant fluid–solid interfacial dynamics in lattice boltzmann simulations. *Journal of Computational Physics, 266*, 161–170.

Willen, D. P., Sierakowski, A. J., Zhou, G., & Prosperetti, A. (2017). Continuity waves in resolved-particle simulations of fluidized beds. *Physical Review Fluids, 2*, Article 114305. https://doi.org/10.1103/PhysRevFluids.2.114305

Yao, Y., Criddle, C. S., & Fringer, O. B. (2021). The effects of particle clustering on hindered settling in high-concentration particle suspensions. *Journal of Fluid Mechanics, 920*, A40. https://doi.org/10.1017/jfm.2021.470

Yin, X., & Koch, D. L. (2007). Hindered settling velocity and microstructure in suspensions of solid spheres with moderate reynolds numbers. *Physics of Fluids, 19*.

Zhang, P., Galindo-Torres, S. A., Tang, H., Jin, G., Scheuermann, A., & Li, L. (2016). Lattice Boltzmann simulations of settling behaviors of irregularly shaped particles. *Physical Review E, 93*, Article 062612. https://doi.org/10.1103/PhysRevE.93.062612. URL: https://link.aps.org/doi/10.1103/PhysRevE.93.062612.

Zhao, S., & Zhao, J. (2023). Revolutionizing granular matter simulations by high-performance ray tracing discrete element method for arbitrarily-shaped particles. *Computer Methods in Applied Mechanics and Engineering, 416*, Article 116370. https://doi.org/10.1016/j.cma.2023.116370